An adaptable refinement approach for shell finite element models based on node-dependent kinematics

An Adaptable Refinement Approach for Shell Finite Element Models Based on Node-Dependent Kinematics

G. Li, E. Carrera, M. Cinefra, A. G. de Miguel, A. Pagani, E. Zappino*

MUL[2] Group, Department of Mechanical and Aerospace Engineering, Politecnico di Torino, Corso Duca degli Abruzzi 24, 10129 Torino, Italy.

Abstract

Towards improving the numerical efficiency in the analysis of multi-layered shell structures with the finite element (FE) method, an adaptable two-level mathematical refinement approach is proposed for refined curvilinear shell elements. Based on Carrera Unified Formulation (CUF), the approximation of displacement functions of shell elements can be improved by refining the through-the-thickness assumptions and enriching the shape functions. By using the hierarchical Legendre polynomial expansions (HLE) as shape functions, the element capabilities can be enhanced conveniently without re-meshing. To further increase the numerical efficiency of shell FE models, Node-Dependent Kinematics (NDK) is utilized to implement local kinematic refinements on the selected FE nodes within the domain of interest. The conjunction of NDK with the two-level refinements of the shell FE models leads to an adaptable refinement approach in the analysis of shell structures, which can be used to build FE models with optimal efficiency and high fidelity. The competence of the proposed approach is investigated through numerical studies on laminated shells.

Keywords: shell models, Carrera Unified Formulation, node-dependent kinematics, hierarchical Legendre polynomials

---

*Corresponding author. Tel: +39 011 090 6887, Fax: +39 011 090 6899.
Email address: enrico.zappino@polito.it (E. Zappino)

1. Introduction

Thin-walled structures with curvatures, better known as shells, are vastly used in modern engineering. Shells span over large areas and can hold applied loads effectively, therefore are ideal to act as light-weight structures. A series of shell theories have been suggested, some of which have been widely adopted in structural analyzes. Traditional models include the classical theory based on Kirchhoff–Love assumption [1], the First-Order Shear Deformation Theory (FSDT) [2] built on the Mindlin–Reissner assumption, and a variety of Higher-Order Theories [3, 4, 5]. Carrera [6] suggested a unified formulation (CUF) as a general framework to formulate continuum-based degenerated 2D models. CUF directly deals with the general terms of the approximation theories and leads to compact expressions of the governing equations in a unified form. Both of the two major types of models for laminated structures, namely the Equivalent Single-Layer (ESL) model, and the Layer-wise (LW) model, can be addressed in the framework of CUF.

Based on CUF, refined finite element (FE) models can be conveniently constructed through the *fundamental nuclei* (FNs) , a core unit of the structural stiffness matrix whose form is independent of the kinematics assumptions [7]. The adopted kinematic theories can be treated as the input parameters to the FE analyzes, leading to a variety of models with variable kinematics, in which the order of approximation expansions can be increased until the desired accuracy is achieved [8, 9]. Also, various and miscellaneous approximation theories can be employed to construct plate/shell FE models with high efficiency. Apart from commonly used Taylor series and Lagrange polynomials, the adoption of trigonometric, exponential, and hyperbolic series, as well as Legendre and Chebyshev polynomials, has also been discussed [10, 11]. A best-theory diagram was suggested to choose the most suitable theory for specific structural analyzes [12, 13, 14]. This variable kinematic approach has been extended to multi-field problems [15, 16, 17].

Node-Dependent Kinematics (NDK) is an FE approach proposed recently in the framework of CUF [18, 19, 20]. By relating the kinematic assumptions to the chosen nodes, FE models with variable nodal kinematics can be built conveniently. NDK can be applied in the construction of FE models for concurrent global-local analysis. Naturally, the critical zone with higher-order assumptions can be bridged to the less-critical area modeled with adequate lower-order theories [21]. ESL models and LW kinematics can coexist in the same element, making the FE model numerically optimal under the given accuracy requirements [22]. Besides, LW models can be used to model laminated structures with surface-mounted or embedded patches, such as piezo-electric components [23]. In such cases, NDK can further make the numerical modeling procedure simplified by avoiding the use of 3D elements locally when accurate responses are needed [24, 25].

The p-version elements based on hierarchical polynomials were proposed in the 1970s [26, 27, 28]. Such elements are more efficient than the h-version refinement due to the fast convergence rate and can help to improve the numerical accuracy on a given set of FE meshes. The avoidance of re-meshing is vital to shorten the overall simulation time consumption from the pre-processing phase. Meanwhile, their hierarchical characteristics make that the stiffness matrix of lower-order elements can be reused when an element with higher-order shape functions is built [29, 30]. Recently, this type of functions defined on 2D domains were used as section functions of the refined beam models [31, 32] and were referred to as Hierarchical Legendre Expansions (HLE). Direct employment as shape functions on refined plate elements was reported by Zappino et al. [33]. Another advantage of the p-version 2D shape functions is that they are not sensitive to locking phenomena when the polynomial order is sufficiently high [29, 30, 34, 35, 36, 37]. Compared to the MITC technique (Mixed Interpolation of Tensorial Components [38, 39]), no additional shape functions are needed thus the extra loops in the FE routines and the corresponding time consumption is avoided.

In the framework of CUF, the refinement of the kinematic assumptions and the increase of the order of the FE shape functions can be carried out at the same time with ease. This two-level refinement approach can lead to a broad spectrum of FE models on the given FE meshes. The combination of NDK variable kinematics and p-version elements with HLE shape functions makes a powerful, adaptable approach for engineers to get improved numerical accuracy with controlled computational costs. In the authors' previous work [33], the HLE has been used in combination with NDK on plate element models. In this article, the construction of shell FE models through NDK and HLE is introduced, and the modeling capabilities are examined through numerical assessments on shell structures.

2. Node-Dependent Kinematics shell FE formulation

2.1. Preliminaries

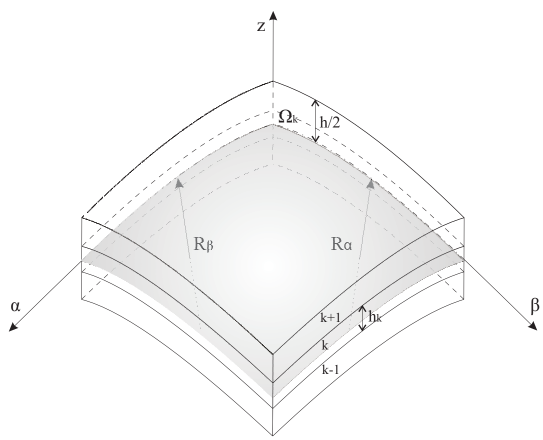

Figure 1: Notation of a shell model for laminated structures.

Shells are thin-walled structures with curvatures in geometry. As illustrated in Fig. 1, a typical shell structure can be described by using the curvilinear reference system (α, β, z), in which α and β indicate the two "in-plane" directions and z the thickness direction. On a shell structure, the infinitesimal in-plane area dS and the infinitesimal volume dV can be expressed as:

$$\begin{aligned} dS &= \quad H_\alpha \, H_\beta \, d\alpha \, d\beta \; = \; H_\alpha \, H_\beta \, d\Omega \; , \\ dV &= \quad H_\alpha H_\beta \, H_z \, d\alpha \, d\beta \, dz \; . \end{aligned} \tag{1}$$

in which $d\Omega$ is the infinitesimal in-plane area on the middle surface of the shell, and the coefficients H_α, H_β and H_z are:

$$H_\alpha = A(1 + z/R_\alpha), \quad H_\beta = B(1 + z/R_\beta), \quad H_z = 1\ . \tag{2}$$

In the above equation, R_α and R_β are the principal radii in the two in-plane directions of the middle surface, A and B the coefficients of the first fundamental form of Ω. For shells with constant curvatures (e.g., cylindrical and spherical shells), $A = B = 1$. In the present work, we consider only shells with constant curvatures. For more details about shell formulations, the reader is referred to [40, 41].

Defined in the curvilinear reference system as shown in Fig. 1, the strain and stress components can be arranged as:

$$\boldsymbol{\epsilon} = \{\epsilon_{\alpha\alpha}, \epsilon_{\beta\beta}, \epsilon_{zz}, \epsilon_{\alpha z}, \epsilon_{\beta z}, \epsilon_{\alpha\beta}\}^T \tag{3}$$

$$\boldsymbol{\sigma} = \{\sigma_{\alpha\alpha}, \sigma_{\beta\beta}, \sigma_{zz}, \sigma_{\alpha z}, \sigma_{\beta z}, \sigma_{\alpha\beta}\}^T \tag{4}$$

The strain vectors $\boldsymbol{\epsilon}$ can be obtained by means of the geometrical relations:

$$\boldsymbol{\epsilon} = \boldsymbol{b}\boldsymbol{u} \tag{5}$$

in which $\boldsymbol{u} = \{u, v, w\}^T$ is the displacement vector, and $\boldsymbol{b}$ is the differential operators matrix, whose explicit expression reads:

$$\boldsymbol{b} = \begin{bmatrix} \frac{\partial_\alpha}{H_\alpha} & 0 & \frac{1}{H_\alpha R_\alpha} \\ 0 & \frac{\partial_\beta}{H_\beta} & \frac{1}{H_\beta R_\beta} \\ 0 & 0 & \partial_z \\ \partial_z - \frac{1}{H_\alpha R_\alpha} & 0 & \frac{\partial_\alpha}{H_\alpha} \\ 0 & \partial_z - \frac{1}{H_\beta R_\beta} & \frac{\partial_\beta}{H_\beta} \\ \frac{\partial_\beta}{H_\beta} & \frac{\partial_\alpha}{H_\alpha} & 0 \end{bmatrix} \tag{6}$$

The stress components can be attained from the constitutive equations as follows:

$$\boldsymbol{\sigma} = \tilde{\boldsymbol{C}}\boldsymbol{\epsilon} \tag{7}$$

in which $\tilde{\boldsymbol{C}}$ is the material coefficients matrix which is obtained by transforming its original form $\boldsymbol{C}$ from the material coordinate system $(1,2,3)$ to the global system (α,β,z). The original $\boldsymbol{C}$ of a single orthotropic lamina in the material system reads:

$$\boldsymbol{C}=\begin{bmatrix} C_{11} & C_{12} & C_{13} & 0 & 0 & 0 \\ C_{21} & C_{22} & C_{23} & 0 & 0 & 0 \\ C_{31} & C_{32} & C_{33} & 0 & 0 & 0 \\ 0 & 0 & 0 & C_{44} & 0 & 0 \\ 0 & 0 & 0 & 0 & C_{55} & 0 \\ 0 & 0 & 0 & 0 & 0 & C_{66} \end{bmatrix} \tag{8}$$

The orthotropic material coefficients are characterized by nine independent coefficients, namely the Young's moduli, the shear moduli, and the Poisson ratios [4].

2.2. Carrera Unified Formulation (CUF) for refined shell models

According to Carrera Unified Formulation (CUF), the displacement field of a shell structure can be assumed to be:

$$\boldsymbol{u}(\alpha,\beta,z)=F_\tau(z)\boldsymbol{u}_\tau(\alpha,\beta) \tag{9}$$

in which $\boldsymbol{u}_\tau(\alpha,\beta)$ is the in-plane displacement vector, and $F_\tau(z)$ are related to the theories of shell structures. The repeated index τ implies the application of Einstein's summation convention. The separation of variables provides the convenience to build a variety of bi-dimensional models for shell structures as elaborated in [7, 9, 10]. When higher-order polynomials are introduced to the definition of F_τ, refined shell theories are formulated, and better solution accuracy is expected to be obtained. The highest order of $F_\tau(z)$ can be increased gradually until the solutions converge according to the chosen threshold.

Since $F_\tau(z)$ depends only on the thickness coordinates, they are also known as the thickness functions. When generating ESL models, $F_\tau(z)$ is expressed on the whole through-the-thickness domain of the multi-layered shells ($z \in [-\frac{h}{2}, \frac{h}{2}]$,

h being the shell thickness), as illustrated in Fig. 2(a). Alternatively, for LW models, the displacements can be written as:

$$\boldsymbol{u}^k(\alpha, \beta, \zeta_k) = F_\tau^k(\zeta_k)\boldsymbol{u}_\tau^k(\alpha, \beta) \tag{10}$$

where $-1 \leq \zeta_k \leq 1$ is the adimensional thickness coordinate within layer k, as shown in Fig. 2(b). The displacement continuity conditions should be enforced at the layer interfaces in this case.

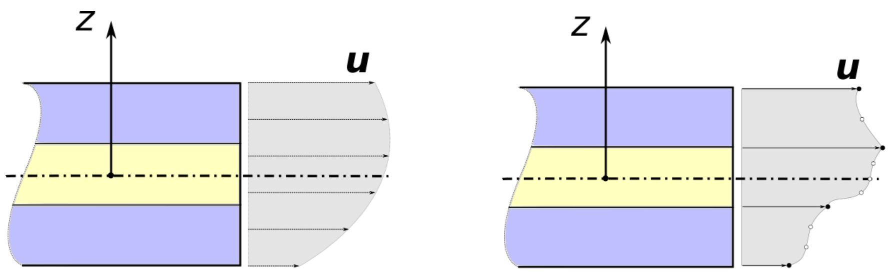

(a) Equivalent Single-Layer (ESL) model

(b) Layer-Wise (LW) model

Figure 2: Two frameworks of models for multi-layered structures.

2.2.1. ESL models based on Taylor expansions (TE)

Taylor series $F_\tau = z^\tau$ can be adopted as thickness functions to build a set of ESL models. In numerical analyzes, if the highest order of the Taylor series is N, then there will be $N + 1$ terms, which read:

$$F_0 = z^0 = 1, \quad F_1 = z^1, \quad \ldots, \quad F_N = z^N \tag{11}$$

Such a 2D model can be denoted as TEN. FSDT [2] can be treated as a particular case of the complete linear model TE1. TE theories are the most commonly used in structural analyzes due to their inherent simplicity. Most times, they are adequate to get global structural responses such as displacements. While, when applied to heterogeneous structures such as laminated shells, TE theories can not guarantee the continuity of the transverse stresses at layer interfaces.

2.2.2. LW models adopting Lagrange expansions (LE)

If F_τ^k are defined as Lagrange interpolation polynomials through the thickness of layer k, as expressed in Eq. 12, an LW model with LE kinematics can be built:

$$F_\tau^k(\zeta_k) = \prod_{i=0, i\neq s}^{N} \frac{\zeta_k - \zeta_{k_i}}{\zeta_{k_\tau} - \zeta_{k_i}} \tag{12}$$

where ζ_{k_τ} are located at the prescribed interpolation points, which are usually equally spaced through the thickness domain. $\zeta_{k_0} = -1$ and $\zeta_{k_N} = 1$ in the natural reference system represent the bottom and top surfaces of the kth layer, respectively.

To enforce the displacement continuity at the interfaces of two neighboring layers, the following constraint should be introduced:

$$u_t^k = u_b^{k+1}, \qquad k = 1, \cdots, N_l - 1. \tag{13}$$

in which N_l is the total number of layers, and the superscripts t and b stand for the top and bottom surfaces of their corresponding layer. The interfacial continuity of transverse stresses are not guaranteed but can be approximately achieved when enough LE terms are used in each layer as discussed by Carrera et al.[10].

2.3. Node-Dependent Kinematics (NDK)

Shape functions $N_i(\alpha, \beta)$ will be introduced to approximate displacement functions through the following expression when 2D models are discretized into FEs:

$$\boldsymbol{u}_\tau(\alpha, \beta) = N_i(\alpha, \beta)\boldsymbol{u}_{i\tau} \tag{14}$$

thus one obtains:

$$\boldsymbol{u}(\alpha, \beta, z) = N_i(\alpha, \beta)F_\tau(z)\boldsymbol{u}_{i\tau} \tag{15}$$

where $\boldsymbol{u}_{i\tau}$ are the unknowns to be calculated. In Eq. 15, the shape functions N_i and the thickness functions F_τ are independent. Carrera et al. [18, 19, 20] introduced a coupling by relating the thickness functions F_τ to the shape functions N_i through:

$$\boldsymbol{u}(\alpha,\beta,z) = N_i(\alpha,\beta)F^i_\tau(z)\boldsymbol{u}_{i\tau} \tag{16}$$

The difference of Eq. 16 from Eq. 15 is the additional superscript i of N_i, which is the index of the "anchoring" node of F_τ. This definition introduces the dependency of the kinematic assumptions on the FE nodes, namely the Node-Dependent Kinematics (NDK). According to NDK, the displacement field can be approximated through Eq. 17 for ESL models, in which $z \in [-\frac{h}{2}, \frac{h}{2}]$:

$$\begin{aligned} \boldsymbol{u}(\alpha,\beta,z) &= N_i(\alpha,\beta)F^i_\tau(z)\boldsymbol{u}_{i\tau} \qquad \tau = 1,\cdots,n_i; \quad i = 1,\cdots,m. \\ \delta\boldsymbol{u}(\alpha,\beta,z) &= N_j(\alpha,\beta)F^j_s(z)\delta\boldsymbol{u}_{js} \qquad s = 1,\cdots,n_j; \quad j = 1,\cdots,m. \end{aligned} \tag{17}$$

where n_i and n_j are the number of expansions on node i and j, respectively. m is the number of shape functions in the element. The displacement functions of LW models are written in Eq. 18 , where $\zeta_k \in [-1,1]$:

$$\begin{aligned} \boldsymbol{u}^k(\alpha,\beta,\zeta_k) &= N_i(\alpha,\beta)F^{ik}_\tau(\zeta_k)\boldsymbol{u}^k_{i\tau} \qquad \tau = 1,\cdots,n^k_i; \quad i = 1,\cdots,m. \\ \delta\boldsymbol{u}^k(\alpha,\beta,\zeta_k) &= N_j(\alpha,\beta)F^{jk}_s(\zeta_k)\delta\boldsymbol{u}^k_{js} \qquad s = 1,\cdots,n^k_j; \quad j = 1,\cdots,m. \end{aligned} \tag{18}$$

in which n^k_i and n^k_j are the number of adopted LW-type expansions in layer k on the corresponding nodes i and j, respectively. Note that the NDK technique also allows for the dependency of the kinematic models on the layer, which can be useful when special attention should be paid to specific layers.

As mentioned before, thickness functions with an increased order provide the chance to the better approximation of the structure responses. With NDK, the kinematic models can be refined locally on specific nodes which makes it easy to perform a local adaptable kinematic refinement. Different theories of structures will be blended naturally by the nodal shape functions within the element in-plane domain without any special coupling approaches. Meanwhile, no compatibility requirements for different nodal kinematics are needed. In the example shown in Fig. 3, the Q4 (four-node quadrilateral Lagrangian) element owns four different theories on its four nodes.

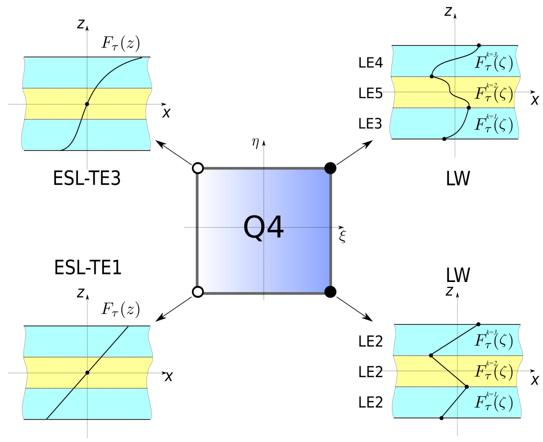

Figure 3: A Q4 element with different nodal kinematics.

The NDK technique can be applied to the efficient global-local modeling of structures. The kinematic model in the critical zone can be refined until the ideal accuracy is achieved while leaving the outlying region modeled with adequate lower-order theories. Global-local FE model can be constructed conveniently without modifying the meshes, and the same set of mesh grids can be re-used to build a family of models for concurrent global-local analyzes. This approach has been used in the efficient modeling of laminated structures in both 1D [18, 20] and 2D [19, 21, 22, 25] cases.

2.4. Hierarchical Legendre Expansions (HLE) as shape functions of 2D elements

A set of shape functions based on Legendre polynomials for a quadrilateral domain $(\xi, \eta) \in [-1, 1]$ was suggested by Szabó et al. [29, 30]. This type of shape functions can be classified into *nodal modes*, *edge modes*, and *internal modes*, as illustrated in Fig. 4.

Nodal modes are defined as Lagrange linear interpolation polynomials on the four vertex nodes of the quadrilateral domain, whose expressions are:

$$N_i(\xi, \eta) = \frac{1}{4}(1 - \xi_i \xi)(1 - \eta_i \eta) \qquad i = 1, 2, 3, 4 \tag{19}$$

in which (ξ_i, η_i) represent the local coordinates of node i in the isoparametric reference system of a quadrilateral element.

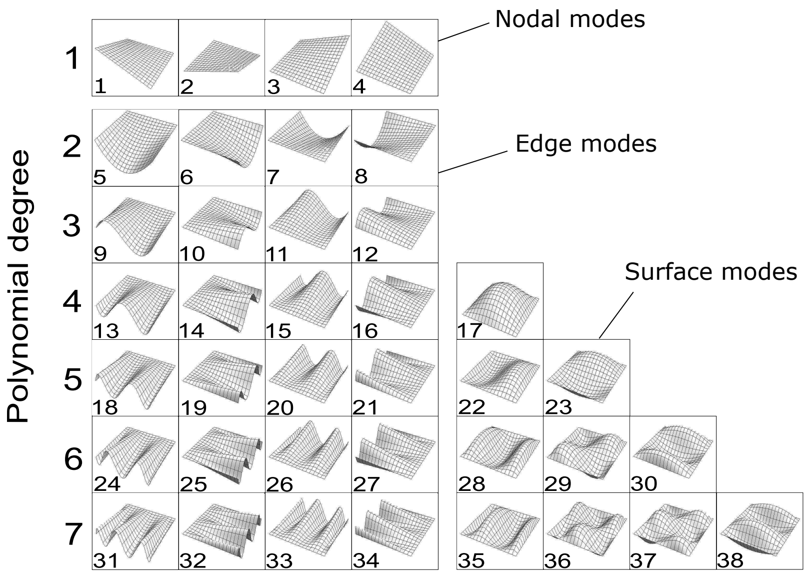

Figure 4: Higher-order Legendre polynomials as shape functions of 2D elements [30].

Edge modes are dominated by the deformation of the four edges and vanish linearly along the perpendicular edges. These functions are expressed as:

$$
\begin{aligned}
N_i(\xi,\eta) &= \frac{1}{2}(1-\eta)\phi_p(\xi) \qquad i = 5, 9, 13, 18, \cdots \\
N_i(\xi,\eta) &= \frac{1}{2}(1+\xi)\phi_p(\eta) \qquad i = 6, 10, 14, 19, \cdots \\
N_i(\xi,\eta) &= \frac{1}{2}(1+\eta)\phi_p(\xi) \qquad i = 7, 11, 15, 20, \cdots \\
N_i(\xi,\eta) &= \frac{1}{2}(1-\xi)\phi_p(\eta) \qquad i = 8, 14, 16, 21, \cdots
\end{aligned} \tag{20}
$$

where ϕ_p is defined as:

$$
\phi_p(\xi) = \sqrt{\frac{2p-1}{2}} \int_{-1}^{\xi} L_{p-1}(x)dx = \frac{L_p(\xi) - L_{p-2}(\xi)}{\sqrt{4p-2}} \qquad p = 2, 3, \cdots \tag{21}
$$

Surface modes contain the deformation shapes that happen on the internal surface and vanish on the edges:

$$
N_i(\xi,\eta) = \phi_m(\xi)\phi_n(\eta) \qquad m, n \geq 2; \quad i = 17, 22, 23, 28, 29, 30, \cdots \tag{22}
$$

With the above hierarchical shape functions, four-node Legendre-type higher-order 2D elements can be formulated. Different from Lagrangian shape functions, when the polynomial degree p increases to $p+1$, only the newly added shape functions and the resulting matrices need to be introduced. Notably, compared with Lagrangian elements of the same polynomial order with equally spaced internal nodes, a fewer number of shape functions are needed. The polynomial order p can be treated as an input parameter, and mathematical enrichment can be conveniently realized on the same meshes to improve the numerical accuracy.

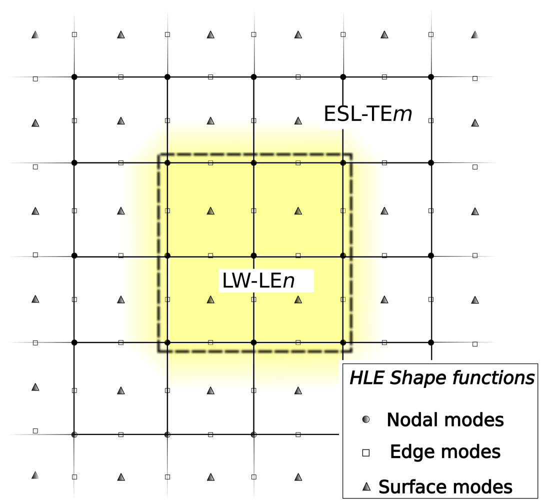

Figure 5: Assignment of nodal kinematics in 2D elements with HLE as shape functions.

For Lagrangian shape functions, each term corresponds to a specific node. While, for HLE shape functions, not every function has a specific position. When NDK is used on HLE-type elements, the “nodes” refer to the indexes of the shape functions directly. Each HLE function can have its individual kinematic model, but for simplicity purposes, in the present work, HLE shape functions of the same mode on the same edge or surface will be assigned to the same kinematic definition, as exhibited in Fig. 5. Determined by the definition of the shape functions, in HLE 2D elements, the “nodal” kinematics will be blended differently from the Lagrangian elements.

2.5. Governing equations of Node-Dependent Kinematic shell FE models

In FE applications, the governing equations of the shell FE models with NDK can be derived from the Principle of Virtual Displacements. For an elastic body in static equilibrium:

$$\delta L_{int} = \delta L_{ext} \tag{23}$$

where δL_{int} is the strain energy, and δL_{ext} the work done by the external loads on the virtual displacements. The internal work can be written as:

$$\delta L_{int} = \int_V \delta \boldsymbol{\epsilon}^T \boldsymbol{\sigma} dV = \int_\Omega \int_{A_k} \delta \boldsymbol{\epsilon}^T \boldsymbol{\sigma} H_\alpha H_\beta \ dz d\Omega \tag{24}$$

in which Ω represents the in-plane domain on the middle surface of the shell, and A_k the thickness domain of layer k.

By considering Eq. 17 or Eq.18 and Eq. 5, the strains can be obtained through the following expression which applies to both ESL and LW models:

$$\begin{aligned} \boldsymbol{\epsilon} &= \boldsymbol{b} N_i F_\tau^{i(k)} \boldsymbol{u}_{i\tau}^{(k)} \\ \delta \boldsymbol{\epsilon} &= \boldsymbol{b} N_j F_s^{j(k)} \boldsymbol{u}_{js}^{(k)} \end{aligned} \tag{25}$$

By substituting the strain expression in Eq. 25 and the constitutive relations in Eq. 7 into Eq. 24, one can get the internal work as:

$$\delta L_{int} = \delta \boldsymbol{u}_{js}^{(k)T} \boldsymbol{K}_{ij\tau s}^k \boldsymbol{u}_{i\tau}^{(k)} \tag{26}$$

where $\boldsymbol{K}_{ij\tau s}^k$ reads:

$$\boldsymbol{K}_{ij\tau s}^k = \int_\Omega \int_{A_k} (\boldsymbol{b} N_j F_s^{j(k)})^T \tilde{\boldsymbol{C}} (\boldsymbol{b} N_i F_\tau^{i(k)}) H_\alpha H_\beta dz d\Omega \tag{27}$$

This 3×3 matrix is the *fundamental nuclei* (FNs) of stiffness in the framework of CUF, the core unit of the element stiffness matrix. It contains nine nucleus components in the form of:

$$\boldsymbol{K}_{ij\tau s}^k = \begin{bmatrix} K_{\alpha\alpha} & K_{\alpha\beta} & K_{\alpha z} \\ K_{\beta\alpha} & K_{\beta\beta} & K_{\beta z} \\ K_{z\alpha} & K_{z\beta} & K_{zz} \end{bmatrix}_{ij\tau s}^k \tag{28}$$

The explicit expressions of the FNs are included in Appendix A.

Assume that $p_z(\alpha, \beta)$ is a distributed load acting on a spatial surface parallel to the middle surface of the shell, the virtual variation of the external work caused by p_z can be expressed as:

$$\delta L_{ext}^{w} = \int_{\Omega} \delta w(z_p)\ p_z\ H_\alpha(z_p)\ H_\beta(z_p)\ d\Omega = \delta w_{js}^{(k)} p_{js}^{z(k)} d\Omega \tag{29}$$

where z_p is the coordinate of the loading surface, and $p_{js}^{z(k)}$ reads:

$$p_{js}^{z(k)} = F_s^{j(k)}(z_p) H_\alpha(z_p)\ H_\beta(z_p)\ \int_{\Omega} N_j\ p_z\ d\Omega \tag{30}$$

By writing the surface load p_z into a vector as $\boldsymbol{p}_z(\alpha, \beta) = \{0, 0, p_z\}^T$, Eq. 29 can be further written into:

$$\delta L_{ext} = \delta \boldsymbol{u}_{js}^{(k)^T} \boldsymbol{P}_{js}^{(k)} \tag{31}$$

where $\boldsymbol{P}_{js}^{(k)} = \{0, 0, p_{js}^{z(k)}\}^T$ are the FNs of the external load. Hence, the governing equations can be obtained as:

$$\delta \boldsymbol{u}_{js}^{(k)^T} : \quad \boldsymbol{K}_{ij\tau s}^{k} \boldsymbol{u}_{i\tau}^{(k)} = \boldsymbol{P}_{js}^{(k)} \tag{32}$$

By looping on the subscripts, the stiffness matrices and the load vector of the shell element can be built step by step. For more details about the assembly technique of FE models in the framework of CUF, see Carrera et al. [7]. In fact, it is straightforward to apply the standard CUF assembly routines to the NDK cases. The work of Zappino et al. [22] contains a discussion on this topic.

3. Numerical examples

Two benchmarks with analytical solutions are first studied for the verification of the proposed HLE shell elements adopting refined kinematics, including two-layered cylindrical shells and a group of spherical shells under distributed pressure. Then, three-layered spherical shells imposed to local bi-sinusoidal pressure are modeled and compared with the 3D FE solutions obtained with the commercial software ABAQUS. Besides the solution accuracy, the computational costs are also compared regarding the total number of degrees of freedom (DOFs) and the relative CPU time $\bar{t}$ consumed in the solution.

In all the three numerical examples, LE kinematics is first used as thickness functions considering the high fidelity of LW models. In the numerical cases, LE kinematics of the same order will be applied to all the layers in a laminated shell. For comparison, TE kinematic theories (including FSDT) are tested. For the thick shells, FE models with Q9 (nine-node quadrilateral Lagrangian element) are assessed. For the thin shells, MITC9 (Q9 with MITC) elements are utilized to mitigate the locking phenomenon in the h-refinement approach when necessary. The related acronyms are included in Appendix B.

3.1. Two-layered cylindrical shells under distributed pressure

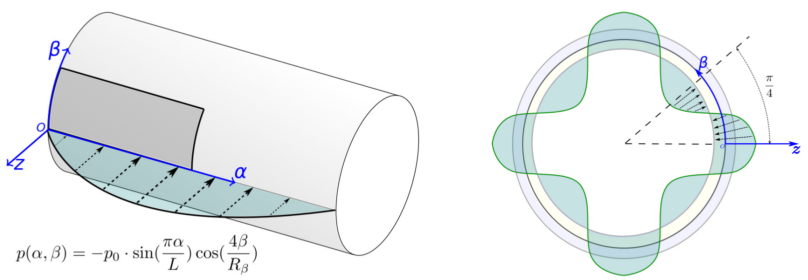

(a) Geometrical feature and axial variattion of the inner pressure load

(b) Sectional profile of the inner pressure load

Figure 6: Geometry and loading of the two-layered cylindrical shells under distributed pressure.

This numerical case refers to the benchmark proposed by Varadan and Bhaskar [42]. The structures are cross-ply cylindrical shells with simple supports on both ends and subjected to transverse distributed pressure on the bottom surface. Fig. 6(a) presents the geometrical features of the structure, the axial variation of the pressure load, and the adopted reference system. Fig. 6(b) illustrates the sectional profile of the inner pressure. The distribution of the inner pressure follows:

$$p(\alpha,\beta) = -p_0 \sin\frac{\pi\alpha}{L}\cos\frac{4\beta}{R_\beta} \tag{33}$$

where L is the length of the shells and R_β the radius of the middle surface, and $L = 4R_\beta$. The circumference of the cylinder is $b = 2\pi R_\beta$, and the total thickness is h. Three different radius-to-thickness ratios are considered, namely $R_\beta/h = 2, 100$, and 500. The considered laminates consist of two plies of equal thickness with stacking sequence $(0°/90°)$ from bottom to top. The material coefficients of the lamina are taken to be: $E_L = 25E_T$, $G_{LT} = 0.5E_T$, $G_{TT} = 0.2E_T$, and $\nu_{LT} = \nu_{TT} = 0.25$, where L and T indicate the longitudinal and transverse direction of the fibers in the lamina, respectively. For comparison purposes, the results are non-dimensionalized through:

$$\bar{w} = -\frac{10E_L h^3}{p_0 R_\beta^4}\ , \quad \bar{\sigma}_{\alpha\alpha} = -\frac{10h^2}{p_0 R_\beta^2}\sigma_{\alpha\alpha}\ , \quad \bar{\sigma}_{\beta\beta} = -\frac{10h^2}{p_0 R_\beta^2}\sigma_{\beta\beta}\ , \quad \bar{\sigma}_{\alpha\beta} = -\frac{10h^2}{p_0 R_\beta^2}\sigma_{\alpha\beta}\ ,$$
$$\bar{\sigma}_{\alpha z} = -\frac{10h}{p_0 R_\beta}\sigma_{\alpha z}\ , \quad \bar{\sigma}_{\beta z} = -\frac{10h}{p_0 R_\beta}\sigma_{\beta z}\ , \quad \bar{\sigma}_{zz} = -\frac{1}{p_0}\sigma_{zz}\ . \tag{34}$$

By making use of the cyclic/symmetric features, a 1/16 FE model can be built which covers 1/2 of the length and 1/8 of the circumference, as represented by the shaded area in Fig. 6(a). The FE models are first refined by increasing the order of thickness functions (F_t and F_s), then by raising the polynomial order of the shape functions (N_i, N_j). When only one element is used in the FE model, obviously HLE1 and HLE2 are not adequate and the p-refinement starts from HLE3 until HLE8. In the final step, the meshing is refined to explore the possibility of further improvement in accuracy.

The obtained results are summarized in Tables 1, 2, and 3. From the numerical results, it can be observed that the combination of refined kinematic shell models and higher order p-version 2D elements can give results with excellent agreement with the reference solutions. As shown in Fig. 7, when sufficiently refined LE models are used, through-the-thickness distribution of $\bar{\sigma}_{\alpha z}$, $\bar{\sigma}_{\beta z}$ are continuous at the interface of the two layers. Also, the variation of $\bar{\sigma}_{zz}$ shows that the shell models adopted are stretchable in the thickness direction. Comparatively, ESL models based on TE lead to good accuracy in the displacements and in-plane stresses but fail in the approximation of out-of-plane stresses. It can also be observed that for the thin shells ($R_\beta/h = 100$ and 500), with LE, a fewer number of expansions can lead to satisfactory results compared with the thick shell case ($R_\beta/h = 2$).

From Tables 2 and 3, it can be found that the transverse shear stresses $\bar{\sigma}_{\alpha z}$ and $\bar{\sigma}_{\beta z}$ obtained through Q9 elements are erroneous even if the meshes are quite refined. The results also manifest that adoption of MITC can effectively overcome this low convergence rate. For the HLE elements, the locking is mitigated by increasing the polynomial order gradually. This is especially obvious for the very thin shell ($R_\beta/h = 500$) whose results in Table 3 show that the HLE3 element is "locked" yet HLE8 is locking free. On the thin shells, the elements adopting higher-order Legendre-type shape functions with refined kinematics perform well and render themselves not sensitive to locking phenomena when the polynomial order is sufficiently high.

Table 1: Displacement and stress evaluation on the two-layered cylindrical shells, $R_\beta/h = 2$.

Theory(F_τ, F_s)	FE(N_i, N_j)	Mesh	$\bar{w}$ $(\frac{L}{2},0,0)$	$\bar{\sigma}_{\alpha\alpha}$ $(\frac{L}{2},0,\frac{h}{2})$	$\bar{\sigma}_{\beta\beta}$ $(\frac{L}{2},0,\frac{h}{2})$	$\bar{\sigma}_{\alpha\beta}$ $(0,\frac{b}{16},\frac{-h}{2})$	$\bar{\sigma}_{\alpha z}$ $(0,0,\frac{-h}{4})$	$\bar{\sigma}_{\beta z}$ $(\frac{L}{2},\frac{b}{16},\frac{h}{4})$	$\bar{\sigma}_{zz}$ $(\frac{L}{2},0,\frac{h}{4})$	DOFs
LE7	Q9	3×6	14.034	0.2517	9.564	-0.5139	0.5016	-3.006	-0.3156	4095
		10×20	14.035	0.2515	9.756	-0.5026	0.4807	-2.938	-0.3132	38745
TE1	HLE8	1×2	13.232	-0.02005	6.653	-0.3233	0.4321	-2.227	-0.4408	510
TE3			13.590	0.2600	9.248	-0.4745	0.4294	-2.689	-0.3261	1020
TE5			13.822	0.2637	9.615	-0.4961	0.4488	-2.832	-0.3129	1530
LE3	HLE3	1×1	15.317	0.4371	8.563	-0.3941	0.3579	-3.131	-0.3359	252
LE4			15.328	0.4085	8.597	-0.3950	0.3586	-3.133	-0.3372	324
LE5			15.343	0.4293	8.685	-0.3954	0.3533	-3.028	-0.3293	396
LE6			15.344	0.4236	8.678	-0.3954	0.3533	-3.028	-0.3291	468
LE7			15.344	0.4257	8.681	-0.3954	0.3543	-3.037	-0.3300	540
LE7	HLE4	1×1	14.002	0.3546	9.981	-0.5257	0.6039	-3.091	-0.2975	765
	HLE5		13.951	0.2609	10.09	-0.5077	0.4706	-2.989	-0.3056	1035
	HLE6		14.034	0.2494	9.762	-0.5029	0.4737	-2.945	-0.3127	1350
	HLE7		14.036	0.2509	9.747	-0.5020	0.4788	-2.934	-0.3133	1710
	HLE8		14.034	0.2514	9.775	-0.5016	0.4787	-2.931	-0.3130	2115
LE7	HLE8	1×2	14.035	0.2514	9.776	-0.5016	0.4786	-2.931	-0.3130	3825
		2×4	14.035	0.2514	9.775	-0.5016	0.4786	-2.931	-0.3130	13005
Varadan and Bhaskar [42]			14.034	0.2511	9.775	-0.5016	0.4786	-2.931	-0.31	

Table 2: Displacement and stress evaluation on the two-layered cylindrical shells, $R_\beta/h = 100$.

Theory(F_τ, F_s)	FE(N_i, N_j)	Mesh	$\bar{w}$	$\bar{\sigma}_{\alpha\alpha}$	$\bar{\sigma}_{\beta\beta}$	$\bar{\sigma}_{\alpha\beta}$	$\bar{\sigma}_{\alpha z}$	$\bar{\sigma}_{\beta z}$	$\bar{\sigma}_{zz}$	DOFs
			$(\frac{L}{2},0,0)$	$(\frac{L}{2},0,\frac{h}{2})$	$(\frac{L}{2},0,\frac{h}{2})$	$(0,\frac{b}{16},\frac{-h}{2})$	$(0,0,\frac{-h}{4})$	$(\frac{L}{2},\frac{b}{16},\frac{h}{4})$	$(\frac{L}{2},0,\frac{h}{4})$	
		6×12	1.359	0.1789	4.764	-0.3455	-0.04168	-7.897	-7.674	6825
LE3	Q9	10×20	1.366	0.1844	5.282	-0.3457	-0.05320	-5.168	-7.956	18081
		15×30	1.367	0.1860	5.438	-0.3455	-0.07126	-4.003	-8.004	39711
		6×12	1.367	0.1882	5.592	-0.3491	-0.1516	-2.989	-7.749	6825
LE3	MITC9	10×20	1.367	0.1875	5.571	-0.3466	-0.1514	-2.979	-7.726	18081
		15×30	1.367	0.1873	5.565	-0.3459	-0.1513	-2.975	-7.717	39711
TE1			1.356	0.2162	5.555	-0.3423	-0.2406	-1.889	50.53	1734
TE3	HLE8	2×4	1.367	0.1868	5.559	-0.3452	-0.2448	-2.284	-6.769	3468
TE5			1.367	0.1867	5.560	-0.3452	-0.1387	-2.820	-5.887	5202
LE1			0.1793	3.61E-03	-2.766	-0.02262	-2.635	5.587	1.990	108
LE2	HLE3	1×1	0.1794	-1.31E-04	-2.772	-0.02262	-2.636	5.589	2.010	180
LE3			0.1794	5.43E-05	-2.772	-0.02262	-2.628	5.481	1.648	252
LE4			0.1794	5.15E-05	-2.772	-0.02262	-2.628	5.481	1.648	324
	HLE4		1.062	0.2123	-8.10E-07	-1.27E-12	23.26	1.127	0.1536	357
	HLE5		1.301	0.2514	9.156	-0.2814	-8.026	-6.152	-8.960	483
LE3	HLE6	1×1	1.361	0.1895	5.889	-0.3670	0.1842	-3.479	-7.704	630
	HLE7		1.366	0.1815	5.217	-0.3467	-0.05745	-2.988	-7.516	798
	HLE8		1.367	0.1867	5.537	-0.3453	-0.1610	-2.989	-7.708	987
		1×2	1.367	0.1872	5.561	-0.3452	-0.1527	-2.975	-7.709	1785
LE3	HLE8	2×4	1.367	0.1872	5.560	-0.3452	-0.1512	-2.972	-7.707	6069
		3×6	1.367	0.1872	5.560	-0.3452	-0.1512	-2.972	-7.707	12873
Varadan and Bhaskar [42]			1.367	0.1871	5.560	-0.3452	-0.1512	-2.972	-7.71	

Table 3: Displacement and stress evaluation on the two-layered cylindrical shells, $R_\beta/h = 500$.

Theory(F_τ, F_s)	FE(N_i, N_j)	Mesh	$\bar{w}$	$\bar{\sigma}_{\alpha\alpha}$	$\bar{\sigma}_{\beta\beta}$	$\bar{\sigma}_{\alpha\beta}$	$\bar{\sigma}_{\alpha z}$	$\bar{\sigma}_{\beta z}$	$\bar{\sigma}_{zz}$	DOFs
			$(\frac{L}{2}, 0, 0)$	$(\frac{L}{2}, 0, \frac{h}{2})$	$(\frac{L}{2}, 0, \frac{h}{2})$	$(0, \frac{b}{16}, \frac{-h}{2})$	$(0, 0, \frac{-h}{4})$	$(\frac{L}{2}, \frac{b}{16}, \frac{h}{4})$	$(\frac{L}{2}, 0, \frac{h}{4})$	
LE3	Q9	10×20	0.1004	0.04390	0.3302	-0.1046	-0.07552	-1.184	-2.990	18081
		15×30	0.1005	0.04447	0.3883	-0.1046	-0.07552	-0.9957	-3.089	39711
LE3	MITC9	10×20	0.1005	0.04500	0.4354	-0.1049	-0.08424	-0.2279	-3.088	18081
		15×30	0.1005	0.04495	0.4349	-0.1047	-0.08417	-0.2276	-3.088	39711
TE1	HLE8	2×4	0.1005	0.04697	0.4367	-0.1044	-0.1216	-0.1482	74.80	1734
TE3			0.1005	0.04508	0.4347	-0.1045	-0.1206	-0.1792	-10.96	3468
TE5			0.1005	0.04477	0.4343	-0.1045	-0.07686	-0.2155	3.165	5202
LE1	HLE3	1×1	7.57E-03	-3.13E-03	-0.7363	-3.73E-03	-2.788	6.174	3.550	108
LE2			7.57E-03	-3.29E-03	-0.7365	-3.73E-03	-2.788	6.174	3.554	180
LE3			7.57E-03	-3.29E-03	-0.7365	-3.73E-03	-2.788	6.169	3.476	252
LE4			7.57E-03	-3.29E-03	-0.7365	-3.73E-03	-2.788	6.169	3.476	324
LE3	HLE4	1×1	0.0629	0.03145	-0.3267	-0.0478	34.49	4.057	18.07	357
	HLE5		0.0905	0.05295	1.353	-0.0789	-12.58	-6.901	-4.191	483
	HLE6		0.1005	0.04709	0.6831	-0.1121	0.32547	-0.8957	-4.138	630
	HLE7		0.1005	0.04424	0.3911	-0.1050	-0.02924	-0.0621	-3.182	798
	HLE8		0.1005	0.04490	0.4323	-0.1045	-0.08594	-0.2232	-3.091	987
LE3	HLE8	1×2	0.1005	0.04491	0.4346	-0.1045	-0.08923	-0.2261	-3.083	1785
		2×4	0.1005	0.04491	0.4345	-0.1045	-0.08410	-0.2274	-3.086	6069
		3×6	0.1005	0.04491	0.4345	-0.1045	-0.08410	-0.2274	-3.086	12873
Varadan and Bhaskar [42]			0.1005	0.0449	0.4345	-0.1045	-0.0841	-0.227	-3.09	

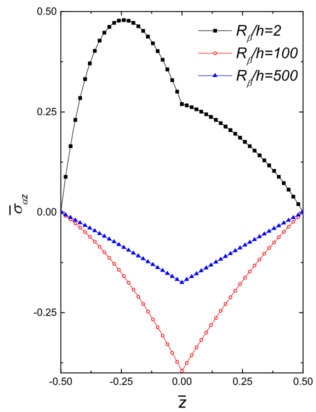

(a) $\bar{\sigma}_{\alpha z}$ through $(0, 0, \bar{z})$

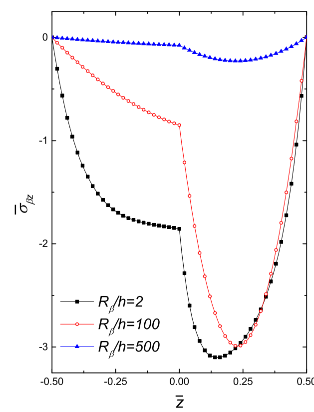

(b) $\bar{\sigma}_{\beta z}$ through $(\frac{L}{2}, \frac{b}{16}, \bar{z})$

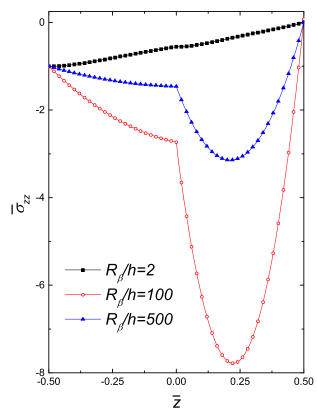

(c) $\bar{\sigma}_{zz}$ through $(\frac{L}{2}, 0, \bar{z})$

Figure 7: Through-the-thickness variation of transverse stresses on the two-layered cylindrical shells ($R_\beta/h = 2$: HLE8-LE7, Mesh=1×2; $R_\beta/h = 100$: HLE8-LE3, Mesh=2×4; $R_\beta/h = 500$: HLE8-LE3, Mesh=2×4).

3.2. *Cross-ply spherical shells under sinusoidally distributed pressure*

This section discusses the bending of cross-ply spherical shells, whose closed-form solutions were provided by Reddy [43]. The mechanical properties of each layer are assumed to be the same as the previous numerical case in Section. 3.1. The in-plane dimensions of the shell middle surface along the α and β axes are assumed to be $a/b = 1.0$, and the radii are considered being $R_\alpha = R_\beta = R$. The structure is subjected to bi-sinusoidally distributed load over the whole middle surface which reads:

$$p(\alpha, \beta) = p_0 \sin \frac{\pi\alpha}{a} \sin \frac{\pi\beta}{b} \tag{35}$$

The shells are simply supported on the four edges by following the boundary conditions as follows:

$$\begin{aligned} \alpha = 0, a: &\quad v = 0, w = 0; \\ \beta = 0, b: &\quad u = 0, w = 0. \end{aligned} \tag{36}$$

Various radius-to-thickness ratios (R/h) and side-to-thickness ratios (a/h) are considered. Laminates with stacking sequences ($0°/90$) and ($0°/90°/90°/0°$) are analyzed. The results are reported regarding only the deflections at the central point ($\frac{a}{2}, \frac{b}{2}, 0$) which are the reference results provided in [43]. The following non-dimensional parameters are used:

$$\bar{w} = \frac{h^3 E_T}{p_0 a^4} w \tag{37}$$

By making use of the symmetric boundary conditions, a 1/4 FE model is built. Table 4 summarizes the results for the two-layered shells with stacking sequence ($0°/90°$) including a thin shell ($a/h = 100$) and a moderate thick one ($a/h = 10$). The same refinement approach used in the last section is again adopted. Thickness functions are first refined, then the order of the HLE elements are gradually increased, while the mesh refinement is considered lastly. The best FE numerical solutions are obtained through LE kinematics and HLE shape functions. Table 5 reports results on the thin shells ($a/h = 100$) with lamination ($0°/90°/90°/0°$) with different radius-to-thickness ratios varying from 1 to 10^{30}. In fact, $R = a \times 10^{30}$ is equivalent to a plate case.

From Tables 4 and 5, it can be observed that the obtained results agree well with the closed-form solutions presented by Reddy [43]. The proposed convergence study procedure leads to models with greatly reduced DOFs compared with the h-refinement with MITC9 elements. It can be found that, if the results are evaluated concerning only displacements ($\bar{w}$), lower-order models can be adequate most times, and higher-order kinematics of either ESL- or LW-type might not be necessary. More detailed comparison of different modeling approaches should be made regarding not only the displacements but also the stresses.

Table 4: Cross-ply spherical shells with $(0°/90°)$ under bi-sinusoidally distributed pressure, $R/h = 5$.

$a/h = 100$					$a/h = 10$				
Theory(F_τ, F_s)	FE(N_i, N_j)	Mesh	$\bar{w}$	DOFs	Theory(F_τ, F_s)	FE(N_i, N_j)	Mesh	$\bar{w}$	DOFs
FSDT	HLE7	1×1	1.1947	190	FSDT	HLE7	1×1	11.181	190
TE1			1.1958	228	TE1			11.189	228
TE3			1.1949	456	TE7			11.406	912
TE5			1.1949	684	TE9			11.411	912
LE2	MITC9	1×1	1.2317	135	LE4	MITC9	1×1	11.528	243
		2×2	1.1981	375			2×2	11.435	675
		4×4	1.1951	1215			4×4	11.427	2187
		8×8	1.1949	4335			8×8	11.427	7803
LE1	HLE2	1×1	0.6374	72	LE1	HLE2	1×1	9.975	72
LE2			0.6377	120	LE2			10.063	120
LE2	HLE3	1×1	1.1054	180	LE3			10.141	168
LE2	HLE4		1.1788	180	LE4			10.141	216
LE2	HLE5		1.1930	345	LE4	HLE3	1×1	10.738	324
LE2	HLE6		1.1950	450	LE4	HLE4		11.334	459
LE2	HLE7		1.1949	570	LE4	HLE5		11.421	621
LE3	HLE7		1.1949	798	LE4	HLE6		11.428	810
LE2	HLE7	2×2	1.1949	1815	LE4	HLE7		11.427	1026
					LE5	HLE7		11.427	1254
					LE4	HLE7	2×2	11.427	3267
Reddy[43]			1.1948		Reddy[43]			11.429	

Table 5: Cross-ply spherical shells with $(0°/90°/90°/0°)$ under bi-sinusoidally distributed pressure, $a/h = 100$.

R/a	Theory(F_τ, F_s)	FE(N_i, N_j)	Mesh	$\bar{w}$	DOFs
1	LE2	HLE7	1×1	0.05323	1026
	LE2	MITC9	8×8	0.05323	7803
	FSDT	HLE7	1×1	0.05322	190
	TE5	HLE7	1×1	0.05323	684
	Reddy[43]			0.0532	
5	LE2	HLE7	1×1	1.0286	1026
	LE2	MITC9	8×8	1.0286	7803
	FSDT	HLE7	1×1	1.0277	190
	TE5	HLE7	1×1	1.0285	684
	Reddy[43]			1.0279	
10^{30}	LE2	HLE7	1×1	4.3463	1026
	LE2	MITC9	4×4	4.3463	7803
	FSDT	HLE7	1×1	4.3327	190
	TE5	HLE7	1×1	4.3451	684
	Reddy[43]			4.3368	

3.3. Simply supported three-layered cross-ply spherical shells under local bi-sinusoidally distributed pressure

This section reports numerical results of simply supported three-layered cross-ply spherical shells subjected to local bi-sinusoidally distributed pressure. The lamination sequence is $(90°/0°/90°)$. The three layers have equal thickness $h/3$. The mechanical properties of each lamina are the same as in Section. 3.1. The geometrical features and loading are illustrated in Fig. 8. The origin point of the curvilinear reference system is placed at the central point of the spherical shells. The middle-surface radii are assumed to be $R_\alpha = R_\beta = R = 1$. The local pressure is subjected to the top surface, and its distribution follows:

$$p(\alpha,\beta) = -p_0 \cos\frac{\pi\alpha}{a/10}\cos\frac{\pi\beta}{b/5} \tag{38}$$

where a and b are dimensions of the spherical shells in α and β direction, respectively. $p_0 = 1$ is the magnitude of the pressure load. The loaded region covers the central area of $\frac{a}{10}\times\frac{b}{5}$. Simple supports are imposed on the four edges, which follow:

$$\begin{aligned} \alpha = \pm\frac{a}{2}: &\quad v = 0, w = 0; \\ \beta = \pm\frac{b}{2}: &\quad u = 0, w = 0. \end{aligned} \tag{39}$$

Radius-to-thickness ratios in a wide range ($R/h = 10, 100, 1000$) are studied. For the convenience of comparison, the deflection and stresses are reported by using the following dimensionless parameters:

$$\begin{aligned} &\bar{w} = -\frac{10^6 E_L h^3}{p_0 R^4} w \ , \quad \bar{\sigma}_{\alpha\alpha} = -\frac{10^4 h^2}{p_0 R^2}\sigma_{\alpha\alpha} \ , \quad \bar{\sigma}_{\beta\beta} = -\frac{10^4 h^2}{p_0 R^2}\sigma_{\beta\beta} \ , \quad \bar{\sigma}_{zz} = -\frac{1}{p_0}\sigma_{zz} \ , \\ &\bar{\sigma}_{\alpha z} = \frac{100h}{p_0 R}\sigma_{\alpha z} \ , \quad \bar{\sigma}_{\beta z} = \frac{100h}{p_0 R}\sigma_{\beta z} \ , \quad \bar{\sigma}_{\alpha\beta} = -\frac{10^5 h^2}{p_0 R^2}\sigma_{\alpha\beta} \ . \end{aligned} \tag{40}$$

By considering the symmetric boundary conditions, a quarter of the structure is modeled. The 1/4 FE model contains 10×10 elements, among which the local pressure load covers the in-plane range of two elements, as illustrated in Fig. 8. The FE models on the given meshes are mathematically enriched until

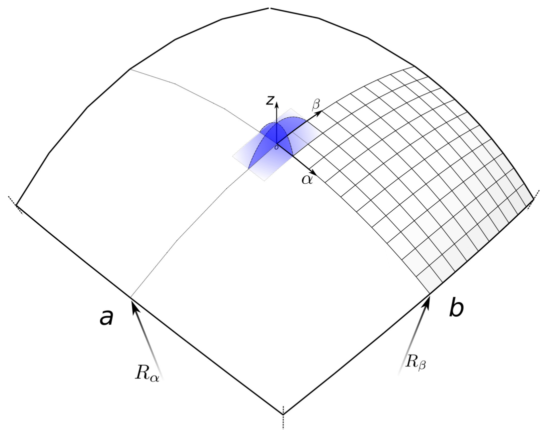

Figure 8: Three-layered cross-ply spherical shells subjected to local bi-sinusoidally distributed pressure.

numerical convergence is achieved with the threshold of 1%. Then, NDK approach is used to construct efficient FE models with local refinement to capture the regional effects caused by the pressure.

For the verification of the adopted refined FE shell models, C3D20R (20-node quadratic brick element with reduced integration) in the commercial software ABAQUS is used to build 3D FE models. It should be noted that for brick elements, the stresses at a node are extrapolated from the integration point values (exact values). Another issue is that the high aspect ratio (span-to-thickness ratio) should be avoided when brick elements are used. Generally, the aspect ratio should not exceed 10 to avoid the potential poor accuracy [44]. Depending on the structural features and the boundary conditions as well as the loading, the high aspect ratios will not necessarily lead to inaccurate results. In the meantime, to obtain detailed stress field, at least five layers of hexahedral elements are used in each lamina in the present work. When the shell becomes thinner, more refined in-lane meshes are needed to reduce the aspect ratio. For the very thin shell with $R/h = 1000$, the effective 3D FE modeling will be very computationally expansive and was not considered. Table 6 summarizes the maximum aspect ratios of the brick elements used in the 3D FE models. It can be found that in the thin shell with $R/h = 100$, one of the 3D models contains elements exceeding the aspect ratio of 10 which is not preferred.

Table 6: Maximum aspect-ratios of C3D20R brick elements in the 3D models for the three-layered spherical shells under local distributed pressure.

R/h	Mesh($\alpha \times \beta \times z$)	Element aspect ratio
10	$50 \times 50 \times 5$	1.7
	$50 \times 50 \times 10$	3.3
100	$50 \times 50 \times 5$	15.8
	$100 \times 100 \times 5$	7.9

The obtained results have been summarized in Tables 7, 8, and 9. The CPU time values $\bar{t}$ listed are relative to the cheapest model (Mesh 10×10, HLE2-LE1). Since the FSDT model is treated as a particular case of TE1 by using a penalty method in the in-house FE code used to collect the numerical results, its CPU time cannot reflect the actual efficiency thus is omitted. Also, for a fair comparison, the CPU time consumptions of ABAQUS 3D models are not listed.

From numerical results in Tables 7 and 8, and the comparison of the transverse shear stresses in Figs. 10 and 11, it can be observed that, when numerical convergence is achieved (through 10×10 elements, HLE5-LE5 for $R/h = 10$, and HLE6-LE4 for $R/h = 100$), great agreement with the C3D20R 3D models is reached, and the maximum relative error is less than 1% for the deflection and the stresses. In fact, 2D elements are free of the aspect ratio problem related to the thickness dimension of thin structures, and the use of CUF empowers the shell elements with adequately refined thickness functions to achieve 3D accuracy. From Tables 7, 8, and 9, it can be found that with the increase of the radius-to-thickness ratio R/h, lower-order LE thickness functions are already sufficient in reaching the convergence. Meanwhile, higher-order shape functions are required to obtain satisfactory results. Since these refinements are mathematical, the re-meshing work (h-version approach) can be reduced to the

Table 7: Deflection and stress evaluation on the three-layered spherical shells under local pressure, $R/h = 10$.

Mesh $(\alpha \times \beta)$	Theory (F_τ, F_s)	Element (N_i, N_j)	$\bar{w}$ (0,0,0)	$\bar{\sigma}_{\alpha\alpha}$ $(0, 0, \frac{h}{6})$	$\bar{\sigma}_{\beta\beta}$ $(0, 0, \frac{h}{2})$	$\bar{\sigma}_{\alpha\beta}$ $(\frac{a}{20}, \frac{b}{10}, \frac{-h}{2})$	$\bar{\sigma}_{\alpha z}$ $(\frac{a}{25}, 0, 0)$	$\bar{\sigma}_{\beta z}$ $(0, \frac{2b}{25}, 0)$	$\bar{\sigma}_{zz}$ $(0, 0, \frac{h}{2})$	Total shape functions	DOFs	CPU time $\bar{t}$
10×10	LE1	HLE2	5607	265.9	425.8	101.2	3.037	1.702	0.8903	341	4092	1.0
	LE2		5669	311.6	512.7	112.4	3.005	1.637	1.088	341	7161	2.0
	LE3		5718	355.6	552.3	117.9	3.506	1.717	1.050	341	10230	3.5
	LE4		5718	356.1	552.4	118.1	3.506	1.716	1.029	341	13299	5.9
	LE5		5719	357.5	550.8	118.2	3.432	1.716	1.024	341	16368	8.6
	LE6		5719	357.4	550.5	118.2	3.433	1.716	1.024	341	19437	11.9
10×10	LE5	HLE3	5722	363.8	539.3	110.8	3.428	1.769	0.9889	561	26928	20.5
		HLE4	5726	361.8	537.4	110.8	3.435	1.771	1.000	881	42288	45.0
		HLE5	5727	361.4	537.5	111.2	3.426	1.770	1.001	1301	62448	88.9
10×10	FSDT	HLE5	5320	365.5	252.7	92.18	2.940	1.104	–	1301	6505	–
	TE1		5290	352.5	264.3	87.24	2.914	1.113	0.5265	1301	7806	3.8
	TE3		5590	274.4	499.9	109.3	3.220	1.512	1.100	1301	15612	14.1
	TE5		5623	257.8	521.8	108.2	3.046	1.577	1.003	1301	23418	31.8
10×10	LE5	MITC9	5724	376.6	565.7	122.7	3.413	1.713	1.030	441	21168	66.3
20×20			5727	367.4	544.2	114.4	3.335	1.770	1.005	1681	80688	308.9
30×30			5727	364.2	540.4	112.7	3.386	1.770	1.002	3721	178608	841.5
40×40			5727	363.0	539.2	112.1	3.426	1.766	1.001	6561	314928	5742.2
50×50			5727	362.4	538.6	111.8	3.453	1.774	1.001	10201	489648	9789.1
10×10	TE1/LE5$^{\times 6}$	HLE5	5522	361.0	543.3	110.5	3.437	1.693	1.001	1301	11922	7.7
	TE1/LE5$^{\times 12}$		5603	360.9	545.7	111.7	3.418	1.739	1.001	1301	15366	11.7
	TE1/LE5$^{\times 20}$		5655	361.4	545.0	111.5	3.421	1.758	1.001	1301	19818	17.4
	TE3/LE5$^{\times 20}$		5694	360.9	538.8	111.2	3.425	1.766	1.001	1301	25908	25.7
	TE5/LE5$^{\times 20}$		5713	361.2	538.2	111.2	3.426	1.770	1.001	1301	31998	41.6
$50 \times 50 \times 5^{\ddagger}$		C3D20R*	5680	349.3	519.7	108.3	3.291	1.744	1.005	162231	486693	–
$50 \times 50 \times 10^{\ddagger}$			5680	358.6	528.2	109.1	3.403	1.757	1.001	316761	950283	–

‡ Mesh $(\alpha \times \beta \times z)$; $*$ ABAQUS 20-node quadratic brick element with reduced integration.

Table 8: Deflection and stress evaluation on the three-layered spherical shells under local pressure, $R/h = 100$.

Mesh $(\alpha \times \beta)$	Theory (F_τ, F_s)	Element (N_i, N_j)	$\bar{w}$ (0,0,0)	$\bar{\sigma}_{\alpha\alpha}$ $(0, 0, \frac{h}{6})$	$\bar{\sigma}_{\beta\beta}$ $(0, 0, \frac{h}{2})$	$\bar{\sigma}_{\alpha\beta}$ $(\frac{a}{20}, \frac{b}{10}, \frac{-h}{2})$	$\bar{\sigma}_{\alpha z}$ $(\frac{a}{25}, 0, 0)$	$\bar{\sigma}_{\beta z}$ $(0, \frac{2b}{25}, 0)$	$\bar{\sigma}_{zz}$ $(0, 0, \frac{h}{2})$	Total shape functions	DOFs	CPU time $\bar{t}$
10×10	LE1	HLE2	185.6	91.53	104.1	52.05	2.145	1.941	2.088	341	4092	1.0
	LE2		186.2	91.61	104.4	52.39	2.154	1.939	1.277	341	7161	1.7
	LE3		186.2	91.52	104.5	52.49	2.712	1.948	1.295	341	10230	3.1
	LE4		186.2	91.52	104.5	52.49	2.712	1.948	1.304	341	13299	4.8
	LE5		186.2	91.52	104.5	52.49	2.706	1.948	1.304	341	16368	7.0
10×10	LE4	HLE3	189.8	111.7	111.0	49.26	2.328	2.386	0.9956	561	21879	11.0
		HLE4	190.1	106.5	109.8	49.17	2.535	2.403	0.9891	881	34359	24.2
		HLE5	190.2	106.0	109.5	49.26	2.493	2.391	0.9994	1301	50739	48.3
		HLE6	190.2	106.2	109.6	49.32	2.483	2.388	1.000	1821	71019	89.2
10×10	FSDT	HLE6	187.0	104.8	107.5	48.26	1.490	0.895	–	1821	9105	–
	TE1		187.2	104.9	107.5	48.26	1.490	0.896	4.022	1821	10926	5.6
	TE3		189.1	105.2	109.6	49.06	1.989	1.727	1.151	1821	21852	20.0
	TE5		189.6	105.5	109.5	49.16	2.062	2.169	0.9900	1821	32778	45.7
10×10	LE4	MITC9	190.0	116.2	114.4	54.20	2.502	2.284	1.123	441	17199	36.6
20×20			190.2	110.8	111.0	50.88	2.357	2.394	1.034	1681	65559	168.4
30×30			190.2	108.4	110.2	50.08	2.426	2.391	1.009	3721	145119	477.4
40×40			190.2	107.5	109.9	49.76	2.488	2.381	1.003	6561	255879	3377.8
50×50			190.2	107.0	109.8	49.61	2.533	2.399	1.001	10201	397839	5875.8
10×10	TE1/LE4$^{\times 6}$	HLE6	190.0	106.2	109.5	49.13	2.482	2.389	1.003	1821	15315	9.3
	TE1/LE4$^{\times 12}$		190.1	106.2	109.5	49.26	2.482	2.389	1.000	1821	19077	13.2
	TE3/LE4$^{\times 12}$		190.2	106.2	109.6	49.31	2.483	2.388	1.000	1821	28521	27.0
$50 \times 50 \times 5^\ddagger$		C3D20R*	192.4	106.7	110.5	49.48	2.463	2.394	0.9886	162231	486693	–
$100 \times 100 \times 5^\ddagger$			192.1	106.4	110.1	49.30	2.459	2.389	1.000	639431	1918293	–

‡ Mesh $(\alpha \times \beta \times z)$; $*$ ABAQUS 20-node quadratic brick element with reduced integration.

Table 9: Deflection and stress evaluation on the three-layered spherical shells under local pressure, $R/h = 1000$.

Mesh $(\alpha \times \beta)$	Theory (F_τ, F_s)	Element (N_i, N_j)	$\bar{w}$ (0,0,0)	$\bar{\sigma}_{\alpha\alpha}$ $(0,0,\frac{h}{6})$	$\bar{\sigma}_{\beta\beta}$ $(0,0,\frac{h}{2})$	$\bar{\sigma}_{\alpha\beta}$ $(\frac{a}{20},\frac{b}{10},\frac{-h}{2})$	$\bar{\sigma}_{\alpha z}$ $(\frac{a}{25},0,0)$	$\bar{\sigma}_{\beta z}$ $(0,\frac{2b}{25},0)$	$\bar{\sigma}_{zz}$ $(0,0,\frac{h}{2})$	Total shape functions	DOFs	CPU time $\bar{t}$
10×10	LE1	HLE2	5.011	5.423	8.499	13.56	1.634	-0.9300	6.446	341	4092	1.0
	LE2		5.012	5.410	8.487	13.56	1.634	-0.9280	2.392	341	7161	1.6
	LE3		5.012	5.410	8.487	13.56	1.678	-0.9279	2.429	341	10230	3.1
	LE4		5.012	5.410	8.487	13.56	1.678	-0.9279	2.433	341	13299	4.7
10×10	LE3	HLE3	5.986	14.16	18.73	11.95	-0.0323	-0.1520	1.094	561	16830	7.3
		HLE4	6.160	15.68	19.01	13.31	-0.5414	0.2285	0.9472	881	26430	15.5
		HLE5	6.216	15.15	17.72	13.24	0.3871	0.5052	0.9819	1301	39030	29.9
		HLE6	6.219	15.12	17.72	13.25	0.3847	0.4946	1.036	1821	54630	72.3
		HLE7	6.219	15.10	17.77	13.25	0.3809	0.4829	1.000	2441	73230	93.1
		HLE8	6.219	15.09	17.76	13.25	0.3865	0.4852	1.000	3161	94830	142.1
10×10	FSDT	HLE8	6.217	15.09	17.77	13.25	0.2336	0.1746	–	3161	15805	–
	TE1		6.227	15.19	17.80	13.25	0.2339	0.1748	36.05	3161	18966	13.9
	TE3		6.218	15.09	17.77	13.25	0.3092	0.3449	0.7835	3161	37932	54.1
	TE5		6.218	15.09	17.77	13.25	0.3206	0.4396	1.353	3161	56898	124.5
10×10	LE3	MITC9	6.314	17.56	19.80	14.52	0.4110	0.4424	2.304	441	13230	23.7
20×20			6.227	15.86	18.16	13.65	0.3422	0.4920	1.509	1681	50430	128.2
30×30			6.220	15.43	17.92	13.46	0.3633	0.4861	1.082	3721	111630	380.5
40×40			6.219	15.28	17.85	13.38	0.3903	0.4813	1.018	6561	196830	741.1
50×50			6.219	15.21	17.82	13.34	0.4137	0.4915	1.006	10201	306030	1245.9
10×10	TE1/LE3$^{\times 6}$	HLE8	6.219	15.09	17.76	13.25	0.3865	0.4852	1.004	3161	24270	19.4
	TE1/LE3$^{\times 12}$		6.219	15.09	17.76	13.25	0.3865	0.4852	1.000	3161	28974	24.6

minimum. Fig. 12 shows that the employed refined shell FE models are capable of obtaining 3D stress fields in detail. For the convenience of observation, the thickness dimensions of the thin shells in Fig. 12 are scaled by certain times.

Again, with TE kinematics, the deflection and in-plane stresses are accurate, yet the transverse stresses are not always reliable. If only the global displacement responses are required, TE kinematics are preferred to LE theories mainly due to its relatively low computational costs. Compared to models with HLE elements with equal accuracy, models with MITC9 elements will contain a lot more shape functions and consume longer computational time. From the comparison, it can also be observed that the adopted higher-order HLE elements are not sensitive to locking even for the very thin shell with $R/h = 1000$.

The NDK technique can be employed to construct FE models with variable TE/LE nodal kinematics, in which the refined LE kinematics is only assigned to the nodes within and adjacent to the loaded region. In fact, shells with different radius-to-thickness ratios (R/h) need different locally refined zones to guarantee the accuracy. Fig. 9 compares three models with different local regions, in which TEm represents TE thickness functions of order m, and LEn stands for LE kinematics of order n. The superscripts of LE$n^{\times Ne}$ indicate the number of elements employing the refined theory LEn on all of their subordinate nodes, and their corresponding area has been indicated in Fig. 9. It should be noted that the rest of the nodes in the FE models will adopt TEm assumptions.

The obtained results in Table 7 show that the moderate-thick shell with $R/h = 10$ needs a comparatively large locally refined area, which is NDK model C in Fig. 9(c) with HLE5-TE5/LE5$^{\times 20}$. For the thin and very thin shells, the locally refined area consists of twelve p-version elements is already sufficient, which correspond to NDK model B in Fig. 9(b). The refinement of the TE theories in the non-critical zone also has a great contribution to the accurate approximation of the stresses in the critical region, especially for the thick shell with $R/h = 10$. From the results in Tables 7, 8, and 9, it can be concluded that, compared to the uniformly refined FE models, the NDK models adopted can help reduce the computational costs considerably without sacrificing the accuracy. A detailed comparison of the through-the-thickness variation of transverse shear stresses in Fig. 10 and Fig. 11 also shows the great agreement of results obtained with the NDK models with the uniformly refined models. By comparing Fig. 13 with Fig. 12, it can also be found that the NDK models can reproduce the stress fields of those obtained with uniformly refined FE models with consistency. As shown in Table 10, compared with the uniform kinematic refinements, the NDK model is particularly efficient for the very thin shell ($R/h = 1000$) which leads to a reduction of 69.4% regarding the DOFs and a decrease of 82.7% in the solution time. Even for the thick shell ($R/h = 10$), the solution consumptions can be saved by around 50%.

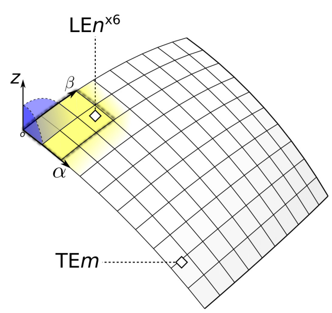

(a) NDK model A: TEm/LE$n^{\times 6}$

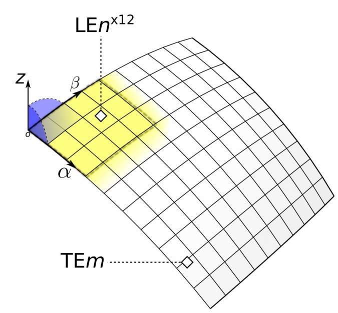

(b) NDK model B: TEm/LE$n^{\times 12}$

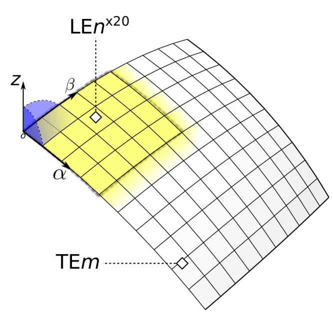

(c) NDK model C: TEm/LE$n^{\times 20}$

Figure 9: NDK models with variable TE/LE nodal capabilities the three-layered spherical shells under local pressure.

Fig.14 reports comprehensive comparisons of different FE models used in the analysis of the spherical shells subjected to local pressure concerning the

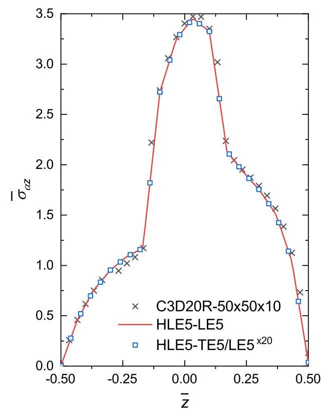

(a) $R/h = 10$

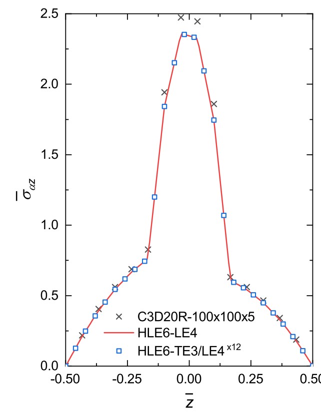

(b) $R/h = 100$

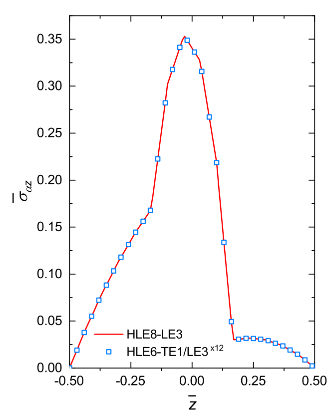

(c) $R/h = 1000$

Figure 10: Through-the-thickness variation of $\bar{\sigma}_{\alpha z}$ through $(\frac{a}{25}, 0, \bar{z})$ on the three-layered spherical shells under local pressure.

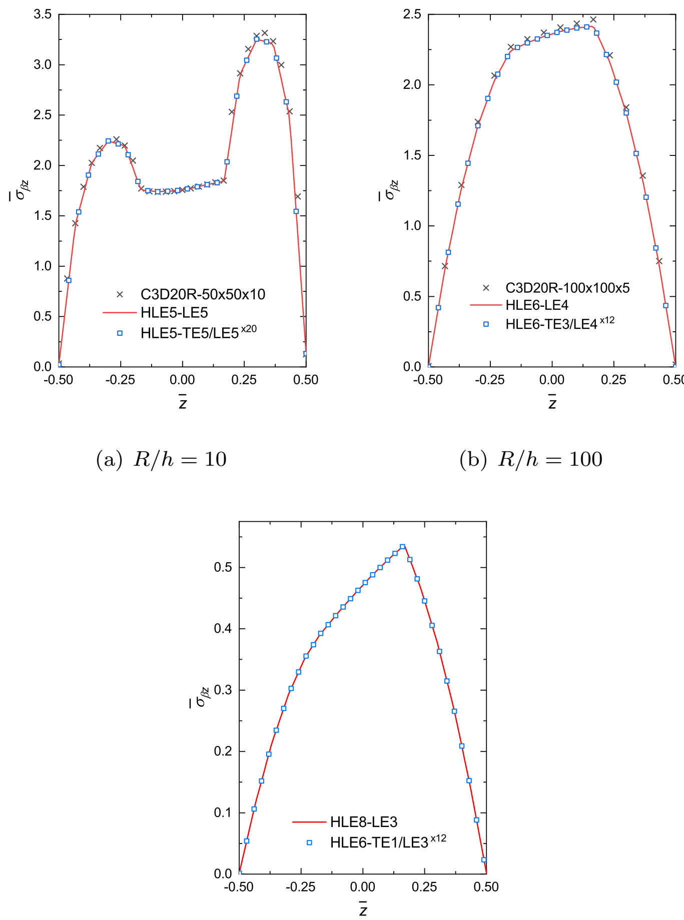

(a) $R/h = 10$

(b) $R/h = 100$

(c) $R/h = 1000$

Figure 11: Through-the-thickness variation of $\bar{\sigma}_{\beta z}$ through $(0, \frac{2b}{25}, \bar{z})$ on the three-layered spherical shells under local pressure.

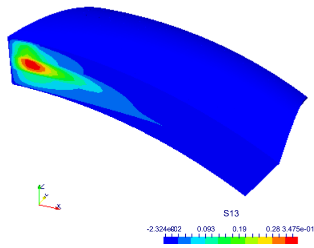

(a) $R/h = 10$, HLE5-LE5, $h \times 1$

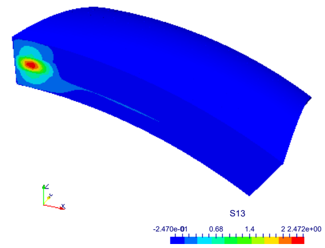

(b) $R/h = 100$, HLE6-LE4, $h \times 10$

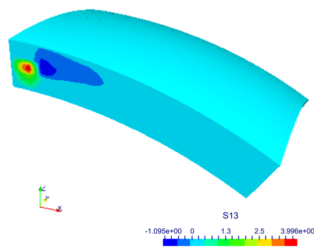

(c) $R/h = 1000$, HLE8-LE3, $h \times 100$

Figure 12: Contour-plots of $\sigma_{\alpha z}$ on the three-layered spherical shells under local pressure, obtained with uniformly refined FE models.

Table 10: A comparison between uniformly refined models and NDK models for the three-layered spherical shells under local pressure regarding computational costs.

R/h	Element	Theory	DOFs	Reduction of DOFs	Relative CPU time $\bar{t}$	Reduction of CPU time
10	HLE5	LE5	62448	–	88.9	–
		TE5/LE5$^{\times 20}$	31998	48.8%	41.6	53.2%
100	HLE6	LE4	71019	–	89.2	–
		TE3/LE4$^{\times 12}$	28521	59.8%	27.0	69.7%
1000	HLE8	LE3	94830	–	142.1	–
		TE1/LE3$^{\times 12}$	28974	69.4%	24.6	82.7%

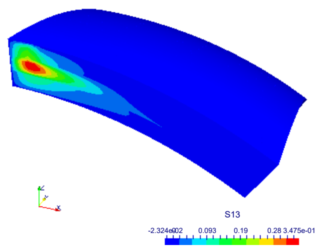

(a) $R/h = 10$, HLE5-TE5/LE5$^{\times 20}$, $h \times 1$

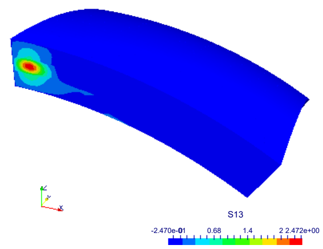

(b) $R/h = 100$, HLE6-TE3/LE4$^{\times 12}$, $h \times 10$

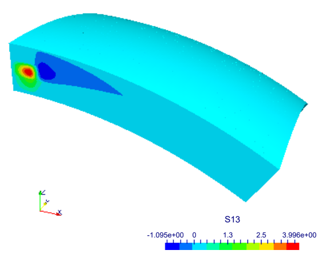

(c) $R/h = 1000$, HLE8-TE1/LE3$^{\times 12}$, $h \times 100$

Figure 13: Contour-plots of $\sigma_{\alpha z}$ on the three-layered spherical shells under local pressure, obtained with NDK FE models.

efficiency. The models listed are those who give the best solutions within their category as stated in Fig.14(a). Considering the DOFs as shown in Fig.14(a), the costs of the C3D20R models increase significantly when the shell gets thinner from $R/h = 10$ to $R/h = 100$. The refined shell elements are much more efficient with comparable accuracy and are less sensitive to the increase of the radius-to-thickness ratio. Compared to the locking-free MITC9 elements, the higher-order HLE elements are also effective in the mitigation of locking and are even more economical. HLE element models with NDK are the most efficient, and the DOFs used for the moderate-thick ($R/h = 10$) and thin ($R/h = 100$) shells take up only 3.4% and 1.5% of DOFs used by C3D20R models, respectively. Fig.14(b) compares the CPU time consumptions of different FE models when solving the equation systems. The MITC9-LE models show a descending trend regarding the CPU time consumption with the decrease of the shell thickness. Differently, HLEp-LE models with uniform kinematic refinement reveal a slightly increasing trend. The efficiency of HLE-NDK models is even more clear concerning the time consumption than the DOFs. For the shells with $R/h = 10, 100$ and 1000, the CPU time consumed in the solution process by HLEp-NDK models takes up only 0.4%, 0.5%, and 2.0% of that spent by the MITC9-LE models, separately. In fact, in engineering simulations, pre-processing, especially meshing takes up most the total work time (e.g., 80%). If the re-meshing work can be simplified or avoided, the simulations can speed up considerably. The proposed HLEp-NDK models can be exploited for this purpose.

4. Conclusions

This paper presents and adaptive refinement approach based on Node-Dependent Kinematics (NDK) for shell finite element (FE) models. Derived from Carrera Unified Formulation (CUF), the proposed models support two levels of mathematical refinements, namely the kinematic refinement with high-fidelity theories, and the refinement of the shape function based on the Hierarchical Legendre polynomial Expansions (HLE). Moreover, NDK technique allows the kinematic

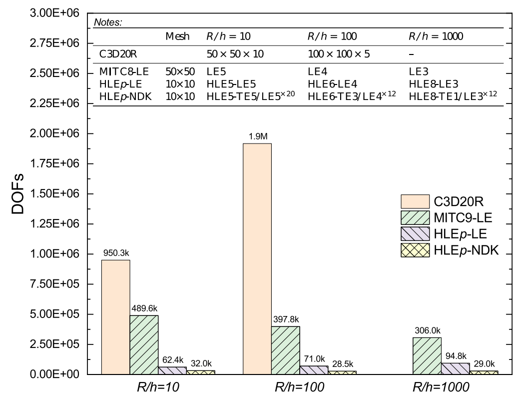

(a) Total number of degrees of freedom (DOFs)

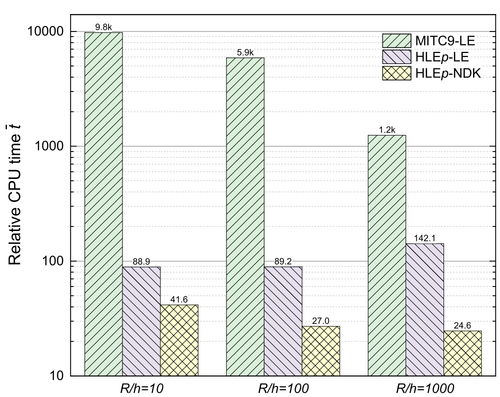

(b) Relative CPU time consumption $\bar{t}$

Figure 14: Comparison of various FE models regarding numerical efficiency in the analysis of the three-layered spherical shells under local pressure.

refinement to be related to the shape functions in the critical region which can be adjustably defined. This adaptable refinement FE approach can help to construct FE models for the analysis of laminated shell structures with optimal efficiency conveniently, and reduce the re-meshing work to the minimum. Through the numerical investigations, the following conclusions can be drawn:

- The two levels of mathematical refinement of FE models, namely the refined kinematics assumption over the shell thickness and the increase of the polynomial degree of the p-version element, empowers one to fully utilize the capabilities of given set of 2D mesh grids in obtaining accurate structural responses with 3D accuracy in an efficient way;
- The locking can be alleviated by increasing the polynomial degree of the HLE shell elements to a sufficiently high order;
- By employing Node-Dependent Kinematics (NDK) technique, a local refinement on the chosen nodes can be carried in an adaptable way, and the computational costs can be further reduced without sacrificing the solution accuracy;
- The appropriately chosen local zone with LW models and he adequately refined ESL kinematics for the non-critical region are both crucial for the successful construction of the NDK FE models.

In summary, the NDK technique can be used to construct refined shell FE models adaptable to the needs of the specific structural analysis. As future work, automatic adaptive routines can be developed for engineering simulations.

5. Acknowledgement

This research work has been carried out within the project FULLCOMP (FULLy analysis, design, manufacturing, and health monitoring of COMPosite structures), funded by the European Union Horizon 2020 Research and Innovation program under the Marie Skłodowska Curie grant agreement No. 642121.

Appendix A Stiffness Fundamental Nuclei (FNs) for Node-Dependent Kinematics shell FE formulations

$$
\begin{aligned}
K_{\alpha\alpha}^{k,ij\tau s} = & \tilde{C}_{11} \triangleleft N_{i,\alpha} N_{j,\alpha} \triangleright_\Omega \triangleleft F_\tau^i F_s^j \frac{H_\beta}{H_\alpha} \triangleright_{A_k} + \tilde{C}_{16} \triangleleft N_{i,\alpha} N_{j,\beta} \triangleright_\Omega \triangleleft F_\tau^i F_s^j \triangleright_{A_k} \\
& + \tilde{C}_{55} \triangleleft N_i N_j \triangleright_\Omega \triangleleft F_{\tau,z}^i F_{s,z}^j H_\alpha H_\beta \triangleright_{A_k} - \tilde{C}_{55} \frac{1}{R_\alpha} \triangleleft N_i N_j \triangleright_\Omega \triangleleft F_\tau^i F_{s,z}^j H_\beta \triangleright_{A_k} \\
& - \tilde{C}_{55} \frac{1}{R_\alpha} \triangleleft N_i N_j \triangleright_\Omega \triangleleft F_{\tau,z}^i F_s^j H_\beta \triangleright_{A_k} + \tilde{C}_{55} \frac{1}{R_\alpha^2} \triangleleft N_i N_j \triangleright_\Omega \triangleleft F_\tau^i F_s^j \frac{H_\beta}{H_\alpha} \triangleright_{A_k} \\
& + \tilde{C}_{16} \triangleleft N_{i,\beta} N_{j,\alpha} \triangleright_\Omega \triangleleft F_\tau^i F_s^j \triangleright_{A_k} + \tilde{C}_{66} \triangleleft N_{i,\beta} N_{j,\beta} \triangleright_\Omega \triangleleft F_\tau^i F_s^j \frac{H_\alpha}{H_\beta} \triangleright_{A_k}
\end{aligned} \tag{A.1}
$$

$$
\begin{aligned}
K_{\alpha\beta}^{k,ij\tau s} = & \tilde{C}_{12} \triangleleft N_{i,\beta} N_{j,\alpha} \triangleright_\Omega \triangleleft F_\tau^i F_s^j \triangleright_{A_k} + \tilde{C}_{26} \triangleleft N_{i,\beta} N_{j,\beta} \triangleright_\Omega \triangleleft F_\tau^i F_s^j \frac{H_\alpha}{H_\beta} \triangleright_{A_k} \\
& + \tilde{C}_{45} \triangleleft N_j N_i \triangleright_\Omega \triangleleft F_{\tau,z}^i F_{s,z}^j H_\alpha H_\beta \triangleright_{A_k} - \tilde{C}_{45} \frac{1}{R_\beta} \triangleleft N_i N_j \triangleright_\Omega \triangleleft F_\tau^i F_{s,z}^j H_\alpha \triangleright_{A_k} \\
& - \tilde{C}_{45} \frac{1}{R_\alpha} \triangleleft N_i N_j \triangleright_\Omega \triangleleft F_{\tau,z}^i F_s^j H_\beta \triangleright_{A_k} + \tilde{C}_{45} \frac{1}{R_\alpha R_\beta} \triangleleft N_i N_j \triangleright_\Omega \triangleleft F_\tau^i F_s^j \triangleright_{A_k} \\
& + \tilde{C}_{16} \triangleleft N_{i,\alpha} N_{j,\alpha} \triangleright_\Omega \triangleleft F_\tau^i F_s^j \frac{H_\beta}{H_\alpha} \triangleright_{A_k} + \tilde{C}_{66} \triangleleft N_{i,\alpha} N_{j,\beta} \triangleright_\Omega \triangleleft F_\tau^i F_s^j \triangleright_{A_k}
\end{aligned} \tag{A.2}
$$

$$
\begin{aligned}
K_{\alpha z}^{k,ij\tau s} = & \tilde{C}_{11} \frac{1}{R_\alpha} \triangleleft N_i N_{j,\alpha} \triangleright_\Omega \triangleleft F_\tau^i F_s^j \frac{H_\beta}{H_\alpha} \triangleright_{A_k} + \tilde{C}_{16} \frac{1}{R_\alpha} \triangleleft N_i N_{j,\beta} \triangleright_\Omega \triangleleft F_\tau^i F_s^j \triangleright_{A_k} \\
& + \tilde{C}_{12} \frac{1}{R_\beta} \triangleleft N_i N_{j,\alpha} \triangleright_\Omega \triangleleft F_\tau^i F_s^j \triangleright_{A_k} + \tilde{C}_{26} \frac{1}{R_\beta} \triangleleft N_i N_{j,\beta} \triangleright_\Omega \triangleleft F_\tau^i F_s^j \frac{H_\alpha}{H_\beta} \triangleright_{A_k} \\
& + \tilde{C}_{13} \triangleleft N_i N_{j,\alpha} \triangleright_\Omega \triangleleft F_{\tau,z}^i F_s^j H_\beta \triangleright_{A_k} + \tilde{C}_{36} \triangleleft N_i N_{j,\beta} \triangleright_\Omega \triangleleft F_{\tau,z}^i F_s^j H_\alpha \triangleright_{A_k} \\
& + \tilde{C}_{55} \triangleleft N_{i,\alpha} N_j \triangleright_\Omega \triangleleft F_\tau^i F_{s,z}^j H_\beta \triangleright_{A_k} - \tilde{C}_{55} \frac{1}{R_\alpha} \triangleleft N_{i,\alpha} N_j \triangleright_\Omega \triangleleft F_\tau^i F_s \frac{H_\beta}{H_\alpha} \triangleright_{A_k} \\
& + \tilde{C}_{45} \triangleleft N_{i,\beta} N_j \triangleright_\Omega \triangleleft F_\tau^i F_{s,z}^j H_\alpha \triangleright_{A_k} - \tilde{C}_{45} \frac{1}{R_\alpha} \triangleleft N_{i,\beta} N_j \triangleright_\Omega \triangleleft F_\tau^i F_s \triangleright_{A_k}
\end{aligned} \tag{A.3}
$$

$$
\begin{aligned}
K^{k,ij\tau s}_{\beta\alpha} &= \tilde{C}_{12} \triangleleft N_{i,\alpha} N_{j,\beta} \triangleright_\Omega \triangleleft F^i_\tau F^j_s \triangleright_{A_k} + \tilde{C}_{16} \triangleleft N_{i,\alpha} N_{j,\alpha} \triangleright_\Omega \triangleleft F^i_\tau F^j_s \frac{H_\beta}{H_\alpha} \triangleright_{A_k} \\
&+ \tilde{C}_{45} \triangleleft N_i N_j \triangleright_\Omega \triangleleft F^i_{\tau,z} F^j_{s,z} H_\alpha H_\beta \triangleright_{A_k} - \tilde{C}_{45} \frac{1}{R_\alpha} \triangleleft N_i N_j \triangleright_\Omega \triangleleft F^i_\tau F^j_{s,z} H_\beta \triangleright_{A_k} \\
&- \tilde{C}_{45} \frac{1}{R_\beta} \triangleleft N_i N_j \triangleright_\Omega \triangleleft F^i_{\tau,z} F^j_s H_\alpha \triangleright_{A_k} + \tilde{C}_{45} \frac{1}{R_\alpha R_\beta} \triangleleft N_i N_j \triangleright_\Omega \triangleleft F^i_\tau F^j_s \triangleright_{A_k} \\
&+ \tilde{C}_{26} \triangleleft N_{i,\beta} N_{j,\beta} \triangleright_\Omega \triangleleft F^i_\tau F^j_s \frac{H_\alpha}{H_\beta} \triangleright_{A_k} + \tilde{C}_{66} \triangleleft N_{i,\beta} N_{j,\alpha} \triangleright_\Omega \triangleleft F^i_\tau F^j_s \triangleright_{A_k}
\end{aligned}
\tag{A.4}
$$

$$
\begin{aligned}
K^{k,ij\tau s}_{\beta\beta} &= \tilde{C}_{22} \triangleleft N_{i,\beta} N_{j,\beta} \triangleright_\Omega \triangleleft F^i_\tau F^j_s \frac{H_\alpha}{H_\beta} \triangleright_{A_k} + \tilde{C}_{26} \triangleleft N_{i,\beta} N_{j,\alpha} \triangleright_\Omega \triangleleft F^i_\tau F^j_s \triangleright_{A_k} \\
&+ \tilde{C}_{44} \triangleleft N_i N_j \triangleright_\Omega \triangleleft F^i_{\tau,z} F^j_{s,z} H_\alpha H_\beta \triangleright_{A_k} - \tilde{C}_{44} \frac{1}{R_\beta} \triangleleft N_i N_j \triangleright_\Omega \triangleleft F^i_\tau F^j_{s,z} H_\alpha \triangleright_{A_k} \\
&- \tilde{C}_{44} \frac{1}{R_\beta} \triangleleft N_i N_j \triangleright_\Omega \triangleleft F^i_{\tau,z} F^j_s H_\alpha \triangleright_{A_k} + \tilde{C}_{44} \frac{1}{R_\beta^2} \triangleleft N_i N_j \triangleright_\Omega \triangleleft F^i_\tau F^j_s \frac{H_\alpha}{H_\beta} \triangleright_{A_k} \\
&+ \tilde{C}_{26} \triangleleft N_{i,\alpha} N_{j,\beta} \triangleright_\Omega \triangleleft F^i_\tau F^j_s \triangleright_{A_k} + \tilde{C}_{66} \triangleleft N_{i,\alpha} N_{j,\alpha} \triangleright_\Omega \triangleleft F^i_\tau F^j_s \frac{H_\beta}{H_\alpha} \triangleright_{A_k}
\end{aligned}
\tag{A.5}
$$

$$
\begin{aligned}
K^{k,ij\tau s}_{\beta z} &= \tilde{C}_{12} \frac{1}{R_\alpha} \triangleleft N_i N_{j,\beta} \triangleright_\Omega \triangleleft F^i_\tau F^j_s \triangleright_{A_k} + \tilde{C}_{16} \frac{1}{R_\alpha} \triangleleft N_i N_{j,\alpha} \triangleright_\Omega \triangleleft F^i_\tau F^j_s \frac{H_\beta}{H_\alpha} \triangleright_{A_k} \\
&+ \tilde{C}_{22} \frac{1}{R_\beta} \triangleleft N_i N_{j,\beta} \triangleright_\Omega \triangleleft F^i_\tau F^j_s \frac{H_\alpha}{H_\beta} \triangleright_{A_k} + \tilde{C}_{26} \frac{1}{R_\beta} \triangleleft N_i N_{j,\alpha} \triangleright_\Omega \triangleleft F^i_\tau F^j_s \triangleright_{A_k} \\
&+ \tilde{C}_{23} \triangleleft N_i N_{j,\beta} \triangleright_\Omega \triangleleft F^i_{\tau,z} F^j_s H_\alpha \triangleright_{A_k} + \tilde{C}_{36} \triangleleft N_i N_{j,\alpha} \triangleright_\Omega \triangleleft F^i_{\tau,z} F^j_s H_\beta \triangleright_{A_k} \\
&+ \tilde{C}_{45} \triangleleft N_{i,\alpha} N_j \triangleright_\Omega \triangleleft F^i_\tau F^j_{s,z} H_\beta \triangleright_{A_k} - \tilde{C}_{45} \frac{1}{R_\beta} \triangleleft N_{i,\alpha} N_j \triangleright_\Omega \triangleleft F^i_\tau F_s \triangleright_{A_k} \\
&+ \tilde{C}_{44} \triangleleft N_{i,\beta} N_j \triangleright_\Omega \triangleleft F^i_\tau F^j_{s,z} H_\alpha \triangleright_{A_k} - \tilde{C}_{44} \frac{1}{R_\beta} \triangleleft N_{i,\beta} N_j \triangleright_\Omega \triangleleft F^i_\tau F_s \frac{H_\alpha}{H_\beta} \triangleright_{A_k}
\end{aligned}
\tag{A.6}
$$

$$
\begin{aligned}
K_{z\alpha}^{k,ij\tau s} = & \tilde{C}_{11}\frac{1}{R_\alpha} \triangleleft N_{i,\alpha}N_j \triangleright_\Omega \triangleleft F_\tau^i F_s^j \frac{H_\beta}{H_\alpha} \triangleright_{A_k} + \tilde{C}_{12}\frac{1}{R_\beta} \triangleleft N_{i,\alpha}N_j \triangleright_\Omega \triangleleft F_\tau^i F_s^j \triangleright_{A_k} \\
& + \tilde{C}_{13} \triangleleft N_{i,\alpha}N_j \triangleright_\Omega \triangleleft F_\tau^i F_{s,z}^j H_\beta \triangleright_{A_k} + \tilde{C}_{55} \triangleleft N_i N_{j,\alpha} \triangleright_\Omega \triangleleft F_{\tau,z}^i F_s^j H_\beta \triangleright_{A_k} \\
& - \tilde{C}_{55}\frac{1}{R_\alpha} \triangleleft N_i N_{j,\alpha} \triangleright_\Omega \triangleleft F_\tau^i F_s^j \frac{H_\beta}{H_\alpha} \triangleright_{A_k} + \tilde{C}_{45} \triangleleft N_i N_{j,\beta} \triangleright_\Omega \triangleleft F_{\tau,z}^i F_s^j H_\alpha \triangleright_{A_k} \\
& - \tilde{C}_{45}\frac{1}{R_\alpha} \triangleleft N_i N_{j,\beta} \triangleright_\Omega \triangleleft F_\tau^i F_s^j \triangleright_{A_k} + \tilde{C}_{16}\frac{1}{R_\alpha} \triangleleft N_{i,\beta}N_j \triangleright_\Omega \triangleleft F_\tau^i F_s^j \triangleright_{A_k} \\
& + \tilde{C}_{26}\frac{1}{R_\beta} \triangleleft N_{i,\beta}N_j \triangleright_\Omega \triangleleft F_\tau^i F_s^j \frac{H_\alpha}{H_\beta} \triangleright_{A_k} + \tilde{C}_{36} \triangleleft N_{i,\beta}N_j \triangleright_\Omega \triangleleft F_\tau^i F_{s,z}^j H_\alpha \triangleright_{A_k}
\end{aligned}
\tag{A.7}
$$

$$
\begin{aligned}
K_{z\beta}^{k,ij\tau s} = & \tilde{C}_{12}\frac{1}{R_\alpha} \triangleleft N_{i,\beta}N_j \triangleright_\Omega \triangleleft F_\tau^i F_s^j \triangleright_{A_k} + \tilde{C}_{22}\frac{1}{R_\beta} \triangleleft N_j N_{i,\beta} \triangleright_\Omega \triangleleft F_\tau^i F_s^j \frac{H_\alpha}{H_\beta} \triangleright_{A_k} \\
& + \tilde{C}_{23} \triangleleft N_{i,\beta}N_j \triangleright_\Omega \triangleleft F_\tau^i F_{s,z}^j H_\alpha \triangleright_{A_k} + \tilde{C}_{45} \triangleleft N_i N_{j,\alpha} \triangleright_\Omega \triangleleft F_{\tau,z}^i F_s^j H_\beta \triangleright_{A_k} \\
& - \tilde{C}_{45}\frac{1}{R_\beta} \triangleleft N_i N_{j,\alpha} \triangleright_\Omega \triangleleft F_\tau^i F_s^j \triangleright_{A_k} + \tilde{C}_{44} \triangleleft N_i N_{j,\beta} \triangleright_\Omega \triangleleft F_{\tau,z}^i F_s^j H_\alpha \triangleright_{A_k} \\
& - \tilde{C}_{44}\frac{1}{R_\beta} \triangleleft N_i N_{j,\beta} \triangleright_\Omega \triangleleft F_\tau^i F_s^j \frac{H_\alpha}{H_\beta} \triangleright_{A_k} + \tilde{C}_{16}\frac{1}{R_\alpha} \triangleleft N_{i,\alpha}N_j \triangleright_\Omega \triangleleft F_\tau^i F_s^j \frac{H_\beta}{H_\alpha} \triangleright_{A_k} \\
& + \tilde{C}_{26}\frac{1}{R_\beta} \triangleleft N_{i,\alpha}N_j \triangleright_\Omega \triangleleft F_\tau^i F_s^j \triangleright_{A_k} + \tilde{C}_{36} \triangleleft N_{i,\alpha}N_j \triangleright_\Omega \triangleleft F_\tau^i F_{s,z}^j H_\beta \triangleright_{A_k}
\end{aligned}
\tag{A.8}
$$

$$
\begin{aligned}
K_{zz}^{k,ij\tau s} = & \tilde{C}_{11}\frac{1}{R_\alpha^2} \triangleleft N_i N_j \triangleright_\Omega \triangleleft F_\tau^i F_s^j \frac{H_\beta}{H_\alpha} \triangleright_{A_k} + 2\tilde{C}_{12}\frac{1}{R_\alpha R_\beta} \triangleleft N_i N_j \triangleright_\Omega \triangleleft F_\tau^i F_s^j \triangleright_{A_k} \\
& + \tilde{C}_{13}\frac{1}{R_\alpha} \triangleleft N_i N_j \triangleright_\Omega \triangleleft F_\tau^i F_{s,z}^j H_\beta \triangleright_{A_k} + \tilde{C}_{22}\frac{1}{R_\beta^2} \triangleleft N_i N_j \triangleright_\Omega \triangleleft F_\tau^i F_s^j \frac{H_\alpha}{H_\beta} \triangleright_{A_k} \\
& + \tilde{C}_{23}\frac{1}{R_\beta} \triangleleft N_i N_j \triangleright_\Omega \triangleleft F_\tau^i F_{s,z}^j H_\alpha \triangleright_{A_k} + \tilde{C}_{13}\frac{1}{R_\alpha} \triangleleft N_i N_j \triangleright_\Omega \triangleleft F_{\tau,z}^i F_s^j H_\beta \triangleright_{A_k} \\
& + \tilde{C}_{23}\frac{1}{R_\beta} \triangleleft N_i N_j \triangleright_\Omega \triangleleft F_{\tau,z}^i F_s^j H_\alpha \triangleright_{A_k} + \tilde{C}_{33} \triangleleft N_i N_j \triangleright_\Omega \triangleleft F_{\tau,z}^i F_{s,z}^j H_\alpha H_\beta \triangleright_{A_k} \\
& + \tilde{C}_{55} \triangleleft N_{i,\alpha}N_{j,\alpha} \triangleright_\Omega \triangleleft F_\tau^i F_s^j \frac{H_\beta}{H_\alpha} \triangleright_{A_k} + \tilde{C}_{45} \triangleleft N_{i,\alpha}N_{j,\beta} \triangleright_\Omega \triangleleft F_\tau^i F_s^j \triangleright_{A_k} \\
& + \tilde{C}_{45} \triangleleft N_{i,\beta}N_{j,\alpha} \triangleright_\Omega \triangleleft F_\tau^i F_s^j \triangleright_{A_k} + \tilde{C}_{44} \triangleleft N_{i,\beta}N_{j,\beta} \triangleright_\Omega \triangleleft F_\tau^i F_s^j \frac{H_\alpha}{H_\beta} \triangleright_{A_k}
\end{aligned}
\tag{A.9}
$$

where $\triangleleft \cdots \triangleright_\Omega$ indicates $\int_\Omega \cdots d\alpha d\beta$, and $\triangleleft \cdots \triangleright_{A_k}$ represents $\int_{A_k} \cdots dz_k$. Ω stands for the middle-surface in-plane domain of the shell element, and A_k

FE(s)	Finite element(s)
CUF	Carrera Unified Formulation
LW	Layer-Wise
ESL	Equivalent Single-Layer
HLE	Hierarchical Legendre polynomial Expansions
NDK	Node-Dependent Kinematics
FSDT	First-Order Shear Deformation Theory
FNs	Fundamental Nuclei
TE	Taylor Expansions
LE	Lagrange Expansions
1D	One-dimensional
2D	Two-dimensional
3D	Three-dimensional
Q4	4-node quadrilateral Lagrangian element
Q9	9-node quadrilateral Lagrangian element
MITC	Mixed Interpolation of Tensorial Components
MITC9	Q9 with Mixed Interpolation of Tonsorial Components
C3D20R	20-node quadratic brick element with reduced integration
DOFs	Degrees of freedom

the thickness domain of layer k.

Appendix B List of acronyms

The following acronyms have been introduced in the text:

References

[1] W. Koiter, On the foundations of the linear theory of thin elastic shell, Proc Kon Nederl Akad Wetensch 73 (3) (1970) 169–195.

[2] P. Naghdi, The theory of plates and shells, Handbuch der Physik, vol. VI a-2 (1972) 425–640.

[3] J. N. Reddy, A simple higher-order theory for laminated composite plates, Journal of Applied Mechanics 51 (4) (1984) 745–752.

[4] J. N. Reddy, Mechanics of laminated composite plates and shells: theory and analysis, CRC Press, 2004.

[5] A. N. Palazotto, Nonlinear analysis of shell structures, AIAA Series, 1992.

[6] E. Carrera, Theories and finite elements for multilayered, anisotropic, composite plates and shells, Archives of Computational Methods in Engineering 9 (2) (2002) 87–140.

[7] E. Carrera, M. Cinefra, M. Petrolo, E. Zappino, Finite element analysis of structures through Unified Formulation, John Wiley & Sons, 2014.

[8] M. Cinefra, E. Carrera, Shell finite elements with different through-the-thickness kinematics for the linear analysis of cylindrical multilayered structures, International Journal for Numerical Methods in Engineering 93 (2) (2013) 160–182.

[9] M. Cinefra, S. Valvano, A variable kinematic doubly-curved MITC9 shell element for the analysis of laminated composites, Mechanics of Advanced Materials and Structures 23 (11) (2016) 1312–1325.

[10] E. Carrera, M. Cinefra, G. Li, G. Kulikov, MITC9 shell finite elements with miscellaneous through-the-thickness functions for the analysis of laminated structures, Composite Structures 154 (2016) 360–373.

[11] E. Carrera, M. Cinefra, G. Li, Refined finite element solutions for anisotropic laminated plates, Composite Structures 183 (2018) 63–76.

[12] M. Petrolo, A. Lamberti, F. Miglioretti, Best theory diagram for metallic and laminated composite plates, Mechanics of Advanced Materials and Structures 23 (9) (2016) 1114–1130.

[13] M. Cinefra, E. Carrera, A. Lamberti, M. Petrolo, Best theory diagrams for multilayered plates considering multifield analysis, Journal of Intelligent Material Systems and Structures 28 (16) (2017) 2184–2205.

[14] J. Yarasca, J. Mantari, M. Petrolo, E. Carrera, Multiobjective best theory diagrams for cross-ply composite plates employing polynomial, zig-zag, trigonometric and exponential thickness expansions, Composite Structures 176 (2017) 860–876.

[15] M. Cinefra, M. Petrolo, G. Li, E. Carrera, Hygrothermal analysis of multilayered composite plates by variable kinematic finite elements, Journal of Thermal Stresses 40 (12) (2017) 1502–1522.

[16] M. Cinefra, M. Petrolo, G. Li, E. Carrera, Variable kinematic shell elements for composite laminates accounting for hygrothermal effects, Journal of Thermal Stresses 40 (12) (2017) 1523–1544.

[17] E. Carrera, S. Valvano, Analysis of laminated composite structures with embedded piezoelectric sheets by variable kinematic shell elements, Journal of Intelligent Material Systems and Structures 28 (20) (2017) 2959–2987.

[18] E. Carrera, E. Zappino, One-dimensional finite element formulation with node-dependent kinematics, Computers & Structures 192 (2017) 114–125.

[19] E. Carrera, A. Pagani, S. Valvano, Multilayered plate elements accounting for refined theories and node-dependent kinematics, Composites Part B: Engineering 114 (2017) 189–210.

[20] E. Carrera, E. Zappino, G. Li, Finite element models with node-dependent kinematics for the analysis of composite beam structures, Composites Part B: Engineering 132 (Supplement C) (2018) 35 – 48.

[21] S. Valvano, E. Carrera, Multilayered plate elements with node-dependent kinematics for the analysis of composite and sandwich structures, Facta Universitatis, Series: Mechanical Engineering 15 (1) (2017) 1–30.

[22] E. Zappino, G. Li, A. Pagani, E. Carrera, Global-local analysis of laminated plates by node-dependent kinematic finite elements with variable ESL/LW capabilities, Composite Structures 172 (2017) 1–14.

[23] M. Cinefra, S. Valvano, E. Carrera, A layer-wise MITC9 finite element for the free-vibration analysis of plates with piezo-patches, International Journal of Smart and Nano Materials 6 (2) (2015) 85–104.

[24] E. Carrera, E. Zappino, G. Li, Analysis of beams with piezo-patches by node-dependent kinematic finite element method models, Journal of Intelligent Material Systems and Structures 29 (7) (2018) 1379–1393.

[25] E. Carrera, S. Valvano, G. Kulikov, Multilayered plate elements with node-dependent kinematics for electro-mechanical problems, International Journal of Smart and Nano Materials (2017) 1–39.

[26] A. Peano, Hierarchies of conforming finite elements for plane elasticity and plate bending, Computers & Mathematics with Applications 2 (3-4) (1976) 211–224.

[27] B. Szabó, A. Mehta, p-convergent finite element approximations in fracture mechanics, International Journal for Numerical Methods in Engineering 12 (3) (1978) 551–560.

[28] O. C. Zienkiewicz, J. D. S. Gago, D. W. Kelly, The hierarchical concept in finite element analysis, Computers & Structures 16 (1) (1983) 53–65.

[29] B. A. Szabó, I. Babuška, Finite element analysis, John Wiley & Sons, 1991.

[30] B. Szabó, A. Düster, E. Rank, The p-Version of the Finite Element Method, Wiley Online Library, 2004.

[31] E. Carrera, A. de Miguel, A. Pagani, Hierarchical theories of structures based on Legendre polynomial expansions with finite element applications, International Journal of Mechanical Sciences 120 (2017) 286–300.

[32] A. Pagani, A. de Miguel, M. Petrolo, E. Carrera, Analysis of laminated beams via Unified Formulation and Legendre polynomial expansions, Composite Structures 156 (2016) 78 – 92, 70th Anniversary of Professor J. N. Reddy.

[33] E. Zappino, G. Li, A. Pagani, E. Carrera, A. de Miguel, Use of higher-order legendre polynomials for multilayered plate elements with node-dependent kinematics, Composite Structures.

[34] B. A. Szabó, Mesh design for the p-version of the finite element method, Computer Methods in Applied Mechanics and Engineering 55 (1-2) (1986) 181–197.

[35] M. Suri, Analytical and computational assessment of locking in the hp finite element method, Computer Methods in Applied Mechanics and Engineering 133 (3-4) (1996) 347–371.

[36] A. Düster, H. Bröker, E. Rank, The p-version of the finite element method for three-dimensional curved thin walled structures, International Journal for Numerical Methods in Engineering 52 (7) (2001) 673–703.

[37] M. Ainsworth, p-and hp-Finite Element Methods. Theory and Applications in Solid and Fluid Mechanics, Mathematics of Computation 70 (235) (2001) 1335–1337.

[38] E. N. Dvorkin, K.-J. Bathe, A continuum mechanics based four-node shell element for general non-linear analysis, Engineering Computations 1 (1) (1984) 77–88.

[39] M. L. Bucalem, K.-J. Bathe, Higher-order mitc general shell elements, International Journal for Numerical Methods in Engineering 36 (21) (1993) 3729–3754.

[40] A. W. Leissa, Vibration of shells, Vol. 288, Scientific and Technical Information Office, National Aeronautics and Space Administration Washington, 1973.

[41] R. M. Jones, Buckling of bars, plates, and shells, Bull Ridge Corporation, 2006.

[42] T. Varadan, K. Bhaskar, Bending of laminated orthotropic cylindrical shells—an elasticity approach, Composite Structures 17 (2) (1991) 141–156.

[43] J. Reddy, Exact solutions of moderately thick laminated shells, Journal of Engineering Mechanics 110 (5) (1984) 794–809.

[44] C. A. Felippa, Introduction to finite element methods, Course Notes, Department of Aerospace Engineeing Sciences, University of Colorado at Boulder, available at http://www. colorado. edu/engineering/Aerospace/CAS/courses. d/IFEM. d.